2192–2212 *Nucleic Acids Research, 2021, Vol. 49, No. 4* *Published online 15 January 2021*
doi: 10.1093/nar/gkaa1277

Another layer of complexity in *Staphylococcus aureus* methionine biosynthesis control: unusual RNase III-driven T-box riboswitch cleavage determines *met* operon mRNA stability and decay

Freya D.R. Wencker [1], Gabriella Marincola [1], Sonja M.K. Schoenfelder [1], Sandra Maaß [2], Dörte Becher [2] and Wilma Ziebuhr [1,*]

[1]Institute of Molecular Infection Biology, University of Würzburg, Würzburg 97080, Germany and [2]Institute of Microbiology, University of Greifswald, Greifswald 17489, Germany

Received September 11, 2020; Revised December 18, 2020; Editorial Decision December 21, 2020; Accepted January 08, 2021

ABSTRACT

In *Staphylococcus aureus, de novo* methionine biosynthesis is regulated by a unique hierarchical pathway involving stringent-response controlled CodY repression in combination with a T-box riboswitch and RNA decay. The T-box riboswitch residing in the 5′ untranslated region (*met* leader RNA) of the *S. aureus metICFE-mdh* operon controls downstream gene transcription upon interaction with uncharged methionyl-tRNA. *met* leader and *metICFE-mdh* (m)RNAs undergo RNase-mediated degradation in a process whose molecular details are poorly understood. Here we determined the secondary structure of the *met* leader RNA and found the element to harbor, beyond other conserved T-box riboswitch structural features, a terminator helix which is target for RNase III endoribonucleolytic cleavage. As the terminator is a thermodynamically highly stable structure, it also forms posttranscriptionally in *met* leader/ *metICFE-mdh* read-through transcripts. Cleavage by RNase III releases the *met* leader from *metICFE-mdh* mRNA and initiates RNase J-mediated degradation of the mRNA from the 5′-end. Of note, *metICFE-mdh* mRNA stability varies over the length of the transcript with a longer lifespan towards the 3′-end. The obtained data suggest that coordinated RNA decay represents another checkpoint in a complex regulatory network that adjusts costly methionine biosynthesis to current metabolic requirements.

GRAPHICAL ABSTRACT

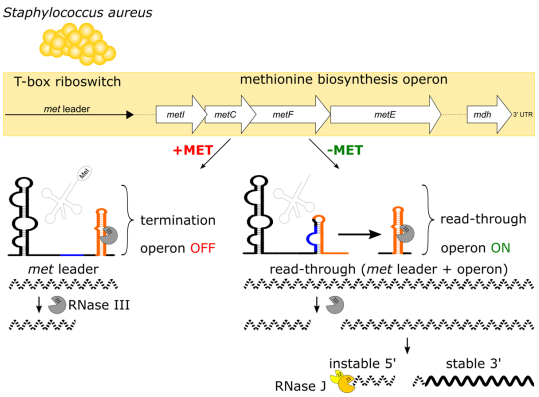

INTRODUCTION

Methionine is the first N-terminal amino acid of nearly all newly synthesized proteins as well as the precursor for the vital methyl group donor *S*-adenosylmethionine (SAM), making the amino acid indispensable for all living organisms. Like many other bacteria, the versatile Gram-positive pathogen *Staphylococcus aureus* is capable of synthesizing methionine *de novo* when the amino acid becomes scarce. The methionine biosynthesis genes in staphylococci are organized in an operon whose size and arrangement is extremely rare among the Bacillales (1,2). Thus, except for *metX*, which is located elsewhere in the genome, the staphylococcal *metICFE-mdh* (*met*) operon encodes all enzymes required for *de novo* methionine biosynthesis, with the gene order matching the single synthesis steps (Figure 1A, B). Methionine is the amino acid with the highest synthesis costs regarding ATP consumption (3). Hence, the pathway is strictly controlled in various microorganisms to avoid methionine accumulation (1,2). Of note, staphylococci have limited metabolic capacities to reuse excess methionine as

*To whom correspondence should be addressed. Tel: +49 931 3182154; Fax: +49 931 3182578; Email: w.ziebuhr@mail.uni-wuerzburg.de

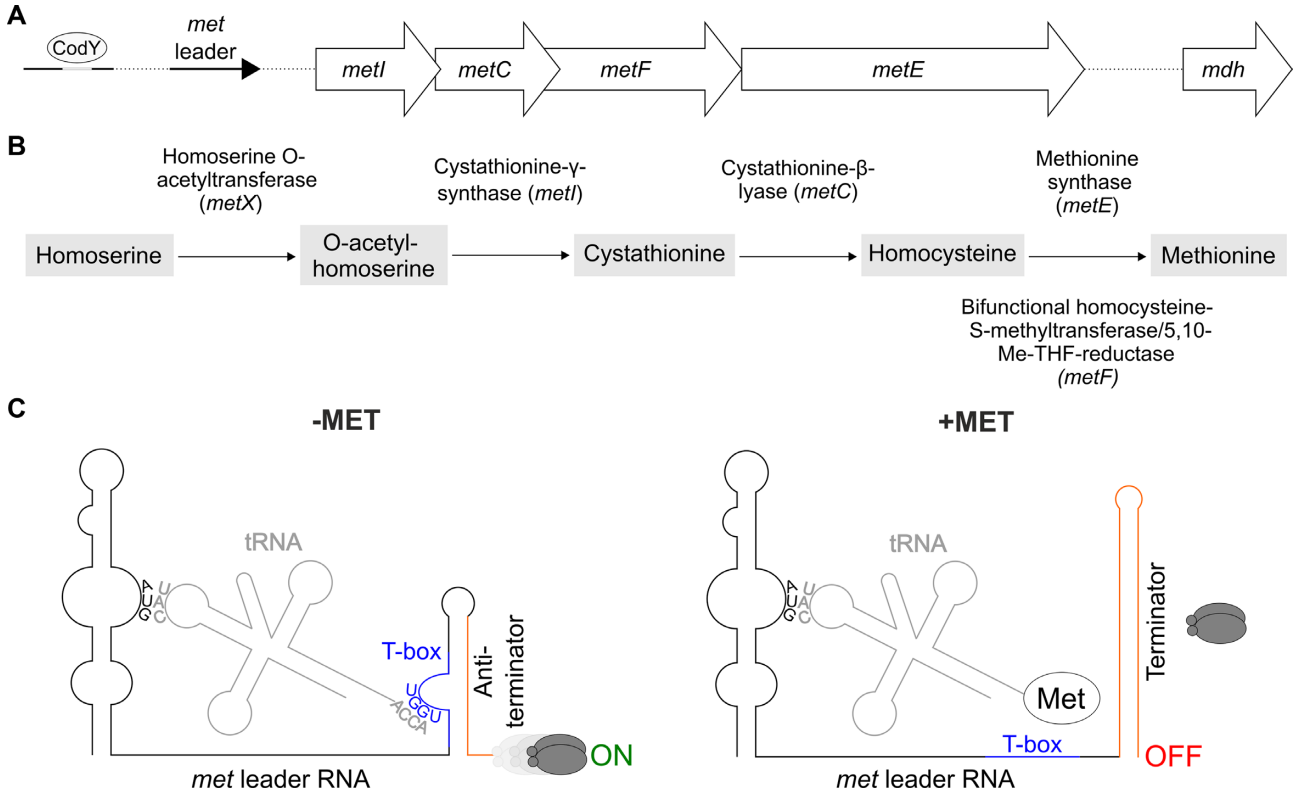

Figure 1. (**A**) Schematic view of the organization of the *S. aureus met* operon including a CodY binding site and its 5′ UTR (*met* leader). (**B**) Methionine biosynthesis pathway in *S. aureus*, Me-THF, methylene-tetrahydrofolate. (**C**) Schematic of the binding interactions between tRNA and *met* leader RNA (T-box riboswitch). Left: system under methionine deprivation ('−MET'), right: system under high intracellular methionine levels ('+MET'). Base pairing of tRNA anticodon ('CAU') with specifier codon ('AUG') of *met* leader and of free 3′ tRNA end ('ACCA') with T-box (depicted in blue) sequence ('UGGU') is shown. Terminator sequence is highlighted in orange, gray ellipses symbolize RNA polymerase, 'ON': read-through into downstream genes, *met* mRNA transcription, 'OFF': premature transcription termination, no *met* mRNA transcription.

they lack methionine salvage and polyamine synthesis to recycle or redirect the amino acid into other pathways, further highlighting the need for effective control of *de novo* methionine biosynthesis in these organisms (4,5). We previously found that methionine biosynthesis in *S. aureus* indeed undergoes extremely tight regulation by a complex hierarchical network (6). Thus, the *met* operon is preceded by a 5′ untranslated region (*met* leader RNA) which represents a T-box riboswitch to control downstream *met* operon transcription. *met* leader RNA transcription itself is under control of the global transcription repressor CodY which in turn is sensitive to amino acid starvation and GTP levels in the cell via (p)ppGpp alarmone production through RelA/SpoT enzymes in a metabolic emergency circuit known as bacterial stringent response (7) (Figure 1A). The combination of stringent response-controlled CodY repressor activity with a T-box riboswitch to regulate gene expression is rare in bacteria, and staphylococcal methionine biosynthesis is further influenced by immediate RNase-mediated decay of *met* operon mRNA after transcription (6).

The crucial checkpoint in this hierarchical string of regulatory events, however, is the T-box riboswitch, which acts in a highly selective and strictly methionine-dependent manner to control *met* operon transcription. T-box riboswitches represent unique RNA-based bacterial transcription control platforms that interact with tRNAs as ligands to regulate downstream gene expression (see references (8,9) for recent reviews). In brief, T-box riboswitches are located in 5′ untranslated regions (UTRs) of genes where they (usually) control transcription by forming either a transcription terminator (system OFF: premature transcription termination) or an antiterminator (system ON: read-through into downstream genes). The ON/ OFF decision of a T-box riboswitch is being made upon binding of either a cognate uncharged or charged tRNA as ligand (Figure 1C). Thus, for example, when methionine is short in supply, methionyl-tRNAs become uncharged and the free 3′-CCA end of the tRNA basepairs with a nucleotide stretch within the 14-nucleotide T-box consensus sequence present in the terminator/antiterminator platform of the T-box riboswitch, resulting in antiterminator formation and ON switch of *met* operon transcription. *Vice versa,* if the 3′-end of the methionyl-tRNA is charged by methionine, no base pairing interaction with the T-box consensus sequence takes place and a terminator stem is formed, causing the RNA polymerase to fall off from its DNA template and to prematurely stop transcription without reading into downstream genes (system OFF) (Figure 1C). Thus, T-box riboswitches represent efficient systems to indirectly sense amino acid levels in the cell by using tRNA charging as a proxy. The tRNA 3′-CCA interaction with the T-box mo-

tif is conserved in all T-box riboswitches, while specificity for a distinct tRNA is usually conferred by interaction of the tRNA anticodon with a cognate codon present in the so-called specifier loop of the riboswitch (Figure 1C). However, other structural elements in the T-box riboswitch were shown to contribute to tRNA recognition and binding as well (10,11).

The T-box riboswitch preceding the *S. aureus met* operon, in the following referred to as *met* leader (RNA), has a number of interesting features. Thus, in comparison to most bacterial T-box riboswitches as well as to other known MET-T-box riboswitches (2,12), the *met* leader is larger in size (i.e. 440 versus ∼250 nt). The difference is mainly due to a long linker region of 226 nucleotides which spans between stem I at the 5′-end and the terminator/antiterminator platform at the 3′-end (6). The function of this exceptionally long linker is currently not known. Other striking features of the system were noticed with respect to *met* leader and *met* operon (m)RNA decay. Thus, upon activation of the *S. aureus met* operon T-box riboswitch, we previously found the *metI* mRNA to undergo rapid degradation immediately after transcription (6). Further, the *met* leader appeared as a distinct RNA species that was short-lived. Initial experiments suggested unexpected involvement of RNase III in *met* leader RNA decay, and of RNase J2 in *met* operon degradation (6). However, the molecular details and the biological significance of these findings remained elusive. Here, we determined the secondary structure of the *met* leader RNA in its OFF state and detected distinct structural elements that recruit RNase III to execute *met* leader RNA cleavage. We identified the exact cleavage site of RNase III within the terminator helix of the riboswitch and found the stability of liberated *met* operon mRNA to vary over the length of the transcript with the mRNA displaying a longer lifespan towards the 3′-end, which was also reflected by corresponding variations in protein amounts. We hypothesize that the uncommon, immediate physical separation of the *met* leader RNA by RNase III initiates targeted *met* operon mRNA decay by RNase J that represents an additional level in the hierarchical methionine biosynthesis control network to adapt enzyme expression to metabolic requirements.

MATERIALS AND METHODS

Bacterial strains and growth conditions

The strains used in this study are listed in Table 1. *Staphylococcus aureus* strains were grown in chemically defined medium (CDM) with (CDM +MET) or without methionine (CDM –MET) described in Supplementary Material 1 when not otherwise stated. For strains carrying resistance genes on cloning vectors, antibiotics were used at the following concentrations for selection: 5 or 10 μg ml^{-1} erythromycin, 10 μg ml^{-1} chloramphenicol. *Staphylococcus aureus* conditional mutants of RNase J2 (*rnjB*::pMUTIN; '$rnjB_{depleted}$') and RNase III (*rnc*::pMUTIN; '$rnc_{depleted}$'), in which the respective RNase genes are under control of an IPTG-inducible promoter, were grown in absence of the inducing agent, rendering the strains functional RNase mutants.

Bacteria from overnight cultures (CDM +MET) were diluted to an initial optical density at 600 nm (OD_{600}) of 0.05 in fresh medium and grown with shaking at 180 rpm at 37°C to mid-exponential growth phase. For methionine-deprived (−MET) conditions bacteria were then washed twice with 1× PBS, resuspended in CDM -MET and incubated for 2 h with shaking at 180 rpm at 37°C.

For rifampicin assays under methionine-deprived conditions, bacteria from overnight cultures were washed twice with 1× PBS, resuspended in 2× basic medium (25 mM Na_2HPO_4, 20 mM KH_2PO_4, 3.3 mM $MgSO_4$, 18.5 mM NH_4Cl, 17 mM NaCl) and diluted to an initial OD_{600} of 0.05 in CDM –MET. Bacteria were grown with shaking at 180 rpm at 37°C to mid-exponential phase.

For protein half-life and synthesis rate determinations bacteria from overnight cultures (CDM +MET) were washed twice with 1x PBS, resuspended in 2× basic medium and diluted in CDM –MET to an initial OD_{600} of 0.05. Bacteria were grown with shaking at 180 rpm at 37°C to mid-exponential growth phase. Then bacteria were washed once with CDM –MET without arginine and lysine and were resuspended in CDM –MET with 1 mM 'heavy' arginine (L-arginine HCl (^{13}C,^{15}N), Silantes GmbH, #201603902) and 'heavy' lysine (L-lysine HCl (^{13}C, ^{15}N), Silantes GmbH, #211603902) (instead of the normal 'light' (^{12}C, ^{14}N) arginine and lysine), t0 sample was taken and methionine or rifampicin was added to a final concentration of 10 mM and 100 μg ml^{-1}, respectively. Bacteria were incubated with shaking at 180 rpm at 37°C. Samples were taken 15, 30, 60 and 240 min after methionine addition (half-life determination) and 15 and 30 min after rifampicin addition (synthesis rate determination), respectively. Samples were put on ice and split in two. One half was immediately pelleted, 1× washed with ice-cold TE-buffer (10 mM Tris (pH 8.0), 1 mM EDTA) supplemented with complete™, EDTA-free Protease Inhibitor Cocktail (Roche, #04693132001) according to manufacturer's instructions, pellet was snap-frozen in liquid nitrogen and stored at −80°C until further processing described under 'Sample Preparation for Proteomics'. The other half of the sample was treated as described for 'Preparation of total RNA'. In addition, the experiment was performed *vice versa* (switch from 'heavy' arginine and lysine to 'light' arginine and lysine containing CDM –MET). The number of biological replicates per time point was 4 (2× 'light' > 'heavy', 2× 'heavy' > 'light'). For the protein quantification experiment, bacteria were resuspended in light medium after washing (no shifting), the t0 sample was taken and processed as described above.

Plasmid and strain construction

All plasmids and oligonucleotides used for this work are listed in Tables 1 and 2, respectively. Details on mutagenesis, cloning and oligonucleotides used for that purpose can be found in Supplementary Method 1 and Tables S1 and S2.

Generation of markerless chromosomally encoded *met* leader mutants

Chromosomal integration of mutated *met* leader sequences was accomplished via allelic replacement with inducible counterselection adapted from Bae & Schneewind using the pBASE6 *S. aureus*/*Escherichia coli* shuttle vector (13,14).

Table 1. Bacterial strains and plasmids

Strain or plasmid	Description	Reference
Strains		
E. coli DC10B	*E. coli* DH10B Δ*dcm* (cytosine methylase deficient) for direct cloning into *S. aureus*	(19)
S. aureus		
RN4220	Restriction-deficient derivative of *S. aureus* 8325-4, cloning host	(20)
Newman	Methicillin-sensitive isolate, NCTC 8178	(21)
Newman 106	RNase J2 mutant, *rnjB*::pMUTIN, Erm(5)	(6)
Newman 107	RNase III mutant, *rnc*::pMUTIN, Erm(5)	(6)
Newman 217	RNase Y mutant, *rny*::*ermC*, Erm(5)	(18)
PR01 (SA564RD Δ*pyrFE*)	*hsdR* type III mutant (restriction deficient), pyrimidine auxotroph	(22)
PR01 ΔRNaseJ1	RNase J1 mutant, Δ*rnjA*, *hsdR* type III mutant, pyrimidine auxotroph	(22)
PR01 ΔRNaseJ2	RNase J2 mutant, Δ*rnjB*, *hsdR* type III mutant, pyrimidine auxotroph	(22)
PR01 ΔRNaseJ1/J2	RNase J1/J2 double mutant, Δ*rnjA*::*ermC*, Δ*rnjB*, *hsdR* type III mutant, pyrimidine auxotroph, Erm(10)	(22)
HG001	Derivative of *S. aureus* 8325-4, *rsbU* restored RN1, *agr* positive	(23,24)
HG001 Δ*rnc*	RNase III mutant, Δ*rnc* region::cat86	(25)
Newman ΔAntiTer&Ter *met* leader	ΔAntiTer&Ter *met* leader mutant	This work
Newman Ter_destab *met* leader	Ter_destab *met* leader mutant	This work
Newman Ter_mutated_1 *met* leader	Ter_mutated_1 *met* leader mutant	This work
Newman Ter_mutated_2 *met* leader	Ter_mutated_2 *met* leader mutant	This work
Newman Ter_mutated_3 *met* leader	Ter_mutated_3 *met* leader mutant	This work
Newman Ter_mutated_4 *met* leader	Ter_mutated_4 *met* leader mutant	This work
Plasmids		
pBASE6	ori pE194ts (temperature-sensitive); ori ColE1; G+/G- shuttle; CmR, AmpR; antisense *secY* under Pxyl/tet promoter	(14)
pBASE_*met* leader+1kb flanking (pFW001)	pBASE6 with wild type *met* leader sequence and 1 kb flanking regions	This work
pBASE_ΔAntiTer&Ter	pFW001 with ΔAntiTer&Ter *met* leader	This work
pBASE_Ter_destab	pFW001 with Ter_destab *met* leader	This work
pGEM-T-easy+Ter_mutated_1	Ter_mutated_1 *met* leader	This work
pBASE6_Ter_mutated_1	pFW001 with Ter_mutated_1 *met* leader	This work
pBASE_Ter_mutated_2	pFW001 with Ter_mutated_2 *met* leader	This work
pBASE_Ter_mutated_3	pFW001 with Ter_mutated_3 *met* leader	This work
pBASE_Ter_mutated_4	pFW001 with Ter_mutated_4 *met* leader	This work
pEB01	ori ColE1 (*E. coli*), ori pT181 (Gram+), *bla* (AmpR), *cat* (CmR), MCS to express gene of interest under native promoter, (pCN47 vector with *ermC* exchanged by *cat*)	(26)
pEB01-*met* leader-*metI*	*met* leader sequence from –35 signal to 5′ region of *metI* (215 nt)	This work
pJC1_tRNAi_deletion	pJC1 with *met* leader, *yfp* and *cI* repressor, deletion of $tRNA_i$ gene	This work

Preparation of total RNA

Total RNA of bacteria was isolated as described previously (15). RNA was precipitated with 4.67× volume ethanol/3 M sodium acetate pH 6.5 (30:1 mix) at −20°C overnight or 1× volume isopropanol and 0.1× volume 3 M sodium acetate pH 6.5 for 10 min at room temperature. Pelleted RNA was washed with 70% ethanol and solved in RNase-free ddH_2O. The quantity was measured with the NanoDrop system (Thermo Scientific, ND-2000). RNA was stored at −80°C.

Northern blot analysis

Unless otherwise specified, 10 μg of total RNA was size separated on 5% denaturing polyacrylamide gels with 7 M urea according to standard procedures. After gel electrophoresis, RNA was transferred onto a nylon membrane (GE Healthcare, Hybond-XL, #RPN203S) using the wet electroblotting technique. RNA was then permanently cross-linked to the membrane by UV light (2 × 120 mJ). For larger mRNA fragments, denaturing 1.2% agarose gels with 1.11% formaldehyde were run in 1x MOPS (3-morpholinopropane-1-sulfonic acid) buffer. Blotting of RNA onto the nylon membrane after electrophoresis was done by classical capillary force technique with 10× SSC buffer (1.5 M NaCl, 150 mM tri-sodium citrate, pH 7.0) overnight or for 2.5 h using the rapid downward transfer method (TurboBlotter™ System, Whatman). RNA was permanently cross-linked by UV light. Membranes were used for hybridization with sequence-specific, radioactively labeled probes. For dsDNA probes, PCR was performed with primer pairs listed in Table 2, and subsequently labeled using Klenow fragment (GE Healthcare, Amersham Megaprime DNA Labeling System, #RPN1606) and [α^{32}P]-dCTP (3000 Ci/mmol, 10 μCi/μl, Hartmann Analytic GmbH, Germany, #SRP-205). Oligonucleotides (ssDNA) listed in Table 2 were 5′-end labeled using T4 polynucleotide kinase (PNK, Thermo Scientific #EK0031) and [γ^{32}P]-ATP (6000 Ci/mmol, 10 μCi/μl, Hartmann Analytic GmbH, Germany, #SRP-501). Hybridization of probes was done in Roti®-Hybri-Quick buffer (Carl Roth GmbH) overnight at 65°C with dsDNA and at 42°C with ssDNA probes. RNA sizes were estimated using the pUC mix marker 8 (Fermentas) as marker for small fragments (100–1000 nucleotides) and *in vitro* transcribed RNAs as ruler for large fragments (1–7.2 kb). Radioactive signals were detected by storage phosphor screens (BAS-IP SR 2040 E) and the Typhoon™ FLA 7000 laser scanner (GE Healthcare).

Table 2. Oligonucleotides

Oligonucleotides			
Purpose	Template	Name	Sequence
cRACE			
met leader	-	FW144	CACTCCAAGGCCATTTTCAA
	-	FW145	GTGATAATTGTTCAGTAAGCAT
metI	-	FW156	CCTGTCGATTGTCCTAGTTT
	-	FW157	CACGTACTAAAAATCCTACA
5′-RACE			
		5′ RACE RNA adapter	CUAGUACUCCGGUAUUGCGGUACCCUUG UACGCCUGUUUUAUA
		5′ RACE RNA adapter primer	GTATTGCGGTACCCTTGT
metI	-	FW200	CGTGGCTGAATGTAAGACTATA
	-	Sa_lgsm02-Lext-Rev	TCAGCACCTTCTGCTAGTGGT
metF	-	FW149	GCGATGTTGAAGTGTGTACGTTT
	-	FW161	CGGTGTGATAATGTATAAACCATT
***ivt* for in-line probing**			
T7 *met* leader	pJC1_tRNAi_deletion	FW088	TTAACTAATACGACTCACTATAGGGTCTTATA ACAGTTTAATGAAACGTAAAC
		Sa.R_met-sRNA	GAAAAAATAAAAAAAGCTTCCGTCCTTCG
T7 short *met* leader	pJC1_tRNAi_deletion	FW130	TTAACTAATACGACTCACTATAGGGATTCTT TACGCACGATTTTTTGTT
		Sa.R_met-sRNA	GAAAAAATAAAAAAAGCTTCCGTCCTTCG
T7 short *met* leader Ter_destab	pBASE_Ter_destab	FW130	TTAACTAATACGACTCACTATAGGGATTCTT TACGCACGATTTTTTGTT
		FW159	GAAAAAATAAAAAAAGAGTCGTTGAATCGT CA
T7 short *met* leader Ter_mutated_1	2.2 kb overlap PCR *met* leader Ter_mutated_1 fragment	FW130	TTAACTAATACGACTCACTATAGGGATTCTT TACGCACGATTTTTTGTT
		FW169	GAAAAAATAAAAAAAGGATCGTTGCCTCGT
T7 short *met* leader Ter_mutated_2	pBASE_Ter_mutated_2	FW130	TTAACTAATACGACTCACTATAGGGATTCTT TACGCACGATTTTTTGTT
		FW211	GAAAAAATAAAAAAAGCTTCCGTGCTTCGT
T7 short *met* leader Ter_mutated_3	pBASE_Ter_mutated_3	FW130	TTAACTAATACGACTCACTATAGGGATTCTT TACGCACGATTTTTTGTT
		FW212	GAAAAAATAAAAAAAGCTTCCGTGCCTCGT
T7 short *met* leader Ter_mutated_4	pBASE_Ter_mutated_4	FW130	TTAACTAATACGACTCACTATAGGGATTCTT TACGCACGATTTTTTGTT
		FW213	GAAAAAATAAAAAAAGCTTCCTGGCTTCGT
dsDNA probes			
met leader	Newman	Sa_lgsm02_Fow	ATGTATTCTAAATGAGTCAGACAACC
		Sa_lgsm02_Rev	CCGTCCTTCGTACCCGAATGA
metI	Newman	Sa_lgsm02-Lext_Fow	ACATCAAGTGGAATGTCAGCCA
		Sa_0431_R	CTATTGGTGAAAGTGTTGCGCCA
metI 5′	Newman	FW137	
		Sa_0431-R_RT	CGAATGATGCAATACCATGCTCA
metC	Newman	Sa_0430_F	GCTCGAACAAATCGAGGGTGCCA
		Sa_0430_R	ACGAAAGCCAATAACGGCAC
metC 3′	Newman	FW140	GCCTCCTTTAATGCGTATTTGAT
		FW141	GCTGATGAGTCTAAAGCACAA
metF	Newman	Sa_0429_F	ACAACTCGTTCAATGTGGTGC
		Sa_0429_R	TCTGCGAGTGTTACCGCATCTAC
metF 3′	Newman	FW138	CTCCTTGTGAGCAGTAATAGATT
		FW139	GGTATTAACACTGACGGTGAT
metE	Newman	Sa_metE_F	TGATGGTCGTAATGTATGGGCA
		Sa_metE_R	CGTTTGTTCTTCCAATCTGCACG
mdh	Newman	FW051	GCAACTTGGGTTGATTTAACGCAT
		FW052	GCCACGAGTTGGTAATTGATCTA
ssDNA probes			
16S rRNA	-	16S_rDNA_R	TACGGCTACCTTGTTACGACTT
5S rRNA	-	5SrRNA	CAGTCCGACTACCATCGGCG

Rifampicin assay for determination of transcript stability

Bacteria were grown to mid-exponential phase as described above. Then rifampicin to a final concentration of 100 μg ml^{-1} was added to the culture. Before (0) and after 0.5, 2, 4, 8, 16 and 32 min of rifampicin exposure, RNA was isolated and Northern blot analyses were performed as described in Supplementary Method 2. Quantification of bands was achieved using the Fiji software (16).

In-line probing

DNA templates that contain the T7 promoter sequence for *in vitro* transcription using the MEGAscript T7 Kit (Ambion, #AM1333) were generated by PCR. Oligos and DNA templates used to generate the individual T7 templates are listed in Table 2. Details about *in vitro* T7 transcription and in-line probing are given in Supplementary Method 3 and Table S3.

Rapid amplification of cDNA ends from circularized RNA (cRACE)

Rapid amplification of cDNA ends from circularized RNA (cRACE) was used to determine 5′- and 3′-ends of the *met* leader transcript as described previously (17). Briefly, DNA-free total RNA was treated with RNA 5′ pyrophosphohydrolase (RppH, NEB, #M0356S) to convert 5′ triphosphate RNA into 5′ monophosphate RNA, to allow for subsequent circularization of transcripts by ligation of 5′- and 3′-ends using T4 RNA ligase (NEB, #M0202). After phenol/chloroform extraction and ethanol precipitation, the circularized RNA was subjected to reverse transcription using a gene-specific primer oriented towards the 5′-end (FW144_cRACE_metleader_fw), followed by PCR amplification (FW144_cRACE_metleader_fw and FW145_cRACE_metleader_rv) (Table 2), cloning of the PCR products into pGEM®-T Easy Vector System I (Promega, #A1360) and transformation into *E. coli* DC10B. 5′-/ 3′-end fusions were analyzed by nucleotide sequencing and mapped to the *met* leader of *S. aureus* strain Newman as reference sequence using the CLC Main Workbench analysis tool (Version 6.6.1; www.clcbio.com).

5′ Rapid amplification of cDNA ends (5′ RACE)

5′ Rapid amplification of cDNA ends (5′ RACE) was performed as described previously (18), but omitting the 5′-triphosphate removal step (by RNA 5′ pyrophosphohydrolase treatment) to exclusively detect processed RNA molecules. Briefly, total RNA was isolated as described above. A specific RNA 5′ adapter (Table 2) was then ligated to the RNA. After phenol/chloroform extraction and ethanol precipitation, the RNA was subjected to reverse transcription using gene-specific primers (for *metI*: FW200, for *metF*: FW161) (Table 2), followed by PCR amplification (for *metI*: Sa_lgsm02-Lext-Rev and 5′ RACE RNA adapter primer, for *metF*: FW149 and 5′ RACE RNA adapter primer) (Table 2) and cloning of the PCR products into pCR-XL-2-TOPO vector (Thermo Fisher Scientific, #K8050) and transformation into *E. coli* DC10B. 5′- ends were analyzed by nucleotide sequencing and mapped to the *met* operon of *S. aureus* strain Newman as reference sequence using the CLC Main Workbench analysis tool (Version 6.6.1; www.clcbio.com).

Sample preparation for proteomics

Cell pellets were resuspended in TE-buffer (50 mM Tris–HCl pH 7.25, 10 mM EDTA) and disrupted with 0.1 mm glass beads and a homogenizer (4 cycles of 30 sec at 6.5 m/s). Between each cycle, samples were placed on ice for 5 min. Glass beads were removed by centrifugation and lysates were subsequently transferred to a new reaction tube. Protein concentration was determined with Roti-Nanoquant (Carl Roth GmbH) according to the manufacturer's protocol. For in solution digest 100 μg protein were reduced with 500 mM tris(2-carboxyethyl)phosphine for 45 min at 65°C and subsequently alkylated with 500 mM iodoacetamide in the dark for 15 min at room temperature before digestion was performed with trypsin (protein-to-enzyme-ratio 200:1) at 37°C for 14 h. Digestion was stopped by lowering the pH to 2 by adding trifluoroacetic acid before samples were desalted via C18 columns (Millipore ZipTips) according to the manufacturer's protocol.

LC–MS/MS measurements

Tryptic peptides were separated by liquid chromatography (LC) and measured online by ESI-mass spectrometry. LC–MS/MS analyses were performed with an EASY-nLC 1200 coupled to an Orbitrap Orbitrap Elite for the half-life and synthesis rate determination or an Orbitrap Velos Pro for the protein quantification (Thermo Fisher Scientific). Peptides were loaded on a self-made analytical column (3 μm particles, Dr Maisch GmbH, OD 360 μm, ID 100 μm, length 20 cm) and eluted by a binary nonlinear gradient of 5–53% acetonitrile in 0.1% acetic acid over 180 min with a flow rate of 300 nl min^{-1}. For MS analysis a full scan in the Orbitrap (m/z 300–1700) with a resolution of 60 000 was followed by CID MS/MS experiments of the twenty most abundant precursor ions acquired in the linear ion trap.

Proteome data processing

Relative protein quantification was achieved using the MaxQuant software (version 1.6.1.0.) (27) and the Andromeda plug-in (28). The *.raw files were searched against a *S. aureus* strain Newman database (downloaded from Uniprot at 15 July 2018, 2584 entries). Additionally, MaxQuant's generic contamination list was included during the search. Database search was performed with following parameters: digestion mode, trypsin/P with up to two missed cleavages; variable modifications, methionine oxidation and acetylation of protein N-termini, a maximal number of five modifications per peptide and activated 'match-between-runs' feature. The false discovery rates of peptide spectrum match and protein were set to 0.01. Only unique peptides were used for protein quantification. The identified proteins from MaxQuant output files were filtered for contaminants, only identified by site and reverse hits with the Perseus software (v. 1.6.1.3). Proteins were accepted if at least two unique peptides could be identified in at least

two of the four biological replicates. The LFQ-values were log_2-transformed, exported and used for statistical analysis using TM4 (29). Statistical significance required a *P*-value <0.01 in an ANOVA applying standard Bonferroni correction. For comparison of protein amounts within one sample, the intensities of all identified peptides were normalized by dividing the respective intensity by the median of all peptide intensities of the same condition. According to Silva *et al*. (30) the normalized intensities of the three most abundant peptides of a proteins were summed to obtain the final quantitative value.

RESULTS

met leader RNA secondary structure

met leader RNA overall organization. To get an insight into the structural constraints of *S. aureus met* operon T-box riboswitch function, we determined the secondary structure of the *met* leader RNA in its OFF- state (i.e. without tRNA ligand) by in-line structural probing (31) (Figure 2A). The approach was augmented by computational folding predictions using the mfold algorithm (32), with experimental data being entered into the program as constraints to eventually build the *met* leader RNA secondary structure model (Figure 2B). Structural probing revealed that the *met* leader RNA harbors typical elements necessary for T-box riboswitch function such as stem I, stem II, stem IIA/B pseudoknot and stem III as well as a terminator helix (Figure 2). In contrast to other T-box riboswitches, however, the *met* leader RNA was found to harbor three additional stem–loops (designated L I–III) that span in a region between stem IIA/B and stem III (Figure 2). Also, a number of minor aberrations within conserved riboswitch elements were detected.

Stem I structural elements. Stem I (nt 27–129) harbors at its base a putative kink-turn element that consists of a typical asymmetric loop flanked by two short helices (Figure 2B). The overall arrangement of the *met* leader kink-turn matches the structures conserved in many T- and S-box riboswitches (9). Other than those elements, however, the kink-turn loop of the *met* leader lacks a 5′-GA-3′ motif that normally flanks the loop at either side (33). Immediately distal from the kink-turn, a canonical specifier loop was identified (nt 42–47 and nt 110–117) which harbors the AUG specifier triplet that is supposed to interact with the anticodon of the cognate met-tRNA (nt 114–116, marked in green in Figure 2B). Immediately 3′ of the AUG specifier codon a conserved purine (G117) is present which, in other T-box riboswitches, was shown to stabilize the specifier codon/ anti-codon interaction (10). Also, the specifier loop of the *met* leader harbors two conserved sequence motifs (marked in yellow in Figure 2B) that are known to undergo weak non-canonical base pairing (9) which is reflected by partial protection of these sequence stretches from degradation in the in-line probing approach (Figure 2A, gels #1–3). Finally, the distal region of stem I carries an AG-bulge (nt 63–71) with a 5′-AGAGA-3′ motif (nt 67–71) and the terminal loop (nt 78–88) with a 5′-GCUGAGA-3′ motif (nt 82–88) (both marked in orange in Figure 2B). These two sequence stretches are highly conserved in T-box riboswitches and were previously shown to undergo base-pairing with each other to form a platform for stem I/tRNA elbow interaction (10,34). In agreement with this function, the regions were found to be protected from degradation during in-line structural probing (Figure 2A, gels # 1 & 2).

Stem II and stem IIA/B pseudoknot. Next to stem I, structural probing demonstrated presence of stem II and a stem IIA/B pseudoknot which are both conserved features in most T-box riboswitches (9). Of note, stem II (nt 133–145) of the *met* leader is unusually short and lacks an S-turn internal loop typical for other T-box riboswitches (Figure 2B) (9). Stem II is followed by a canonical stem IIA/B (nt 150–163) whose apical loop sequence (nt 156–158) base-pairs with a downstream single-stranded stretch (nt 169–171) thereby forming a pseudoknot that is found in many T-box riboswitches (Figure 2A, gel # 3; Figure 2B, nucleotides marked in light blue).

Insertion between stem IIA/B and stem III. The most striking and characteristic feature of the *met* leader is the presence of 150 additional nucleotides (nt 174–323) inserted between the stem IIA/B pseudoknot and stem III (Figure 2B). Structural probing revealed this region to harbor three stem-loops, designated stem L I (nt 174–205), L II (nt 217–283) and L III (nt 293–323) (Figure 2A, gels # 4 & 5). Stem L I is a 10 bp-long helix, carrying an internal 3+2 asymmetric loop (nt 180–182 and 198–199) and a 7-nt apical loop (nt 187–193). Stem L II represents a 22 nt-long helix, with a proximal 4+3 (nt 224–227 and 274–276) and a distal 3+2 (nt 237–239 and 263–264) asymmetric internal loop as well as an A/C mismatch pair (nt 232 & 269). The apical loop of stem L II consists of 11 nt (nt 246–256). Finally, stem L III is a 10 bp-long helix with an 11-nt apical loop (nt 303–313) (Figure 2B). The L I–III elements are absent in all other T-box riboswitches analyzed so far, and presence of this region expands the size of the linker region between stem I and the T-box sequence to 226 nt.

Stem III, T-box and terminator stem. Stem III is a highly conserved T-box riboswitch structure of variable sequence and length (9). Stem III of the *met* leader RNA (nt 330–351) consists of a 9-bp stem and an apical loop of four nucleotides (nt 339–342) (Figure 2A, gel # 5). The structure precedes the T-box sequence (nt 357–370, dark blue in Figure 2B) which forms (in the OFF-state of the *met* leader RNA) a small bulge (nt 361–365) that is stabilized at its base by two consecutive G/C base pairs (Figure 2A, gel # 5; Figure 2B). Downstream of the T-box motif a terminator stem is present which is an essential structural feature of all riboswitches that control downstream genes via transcription termination (Figure 2A gel #5, Figure 2B). The T-box transcription terminator of the *met* leader RNA consists of a 23-bp stem (nt 377–427) with an U/C mismatch pair (nt 392 & 412) and a small 5-bp apical loop (nt 400–404). Of note, the size of the *met* leader terminator stem is longer than most other known T-box riboswitch terminators (12). Also, due to its length and sequence, the *met* leader terminator is a thermodynamically highly stable structure (free energy $\Delta G = -32.60$ kcal/mol). Similar to other T-box systems, the *met* leader terminator harbors seven (conserved)

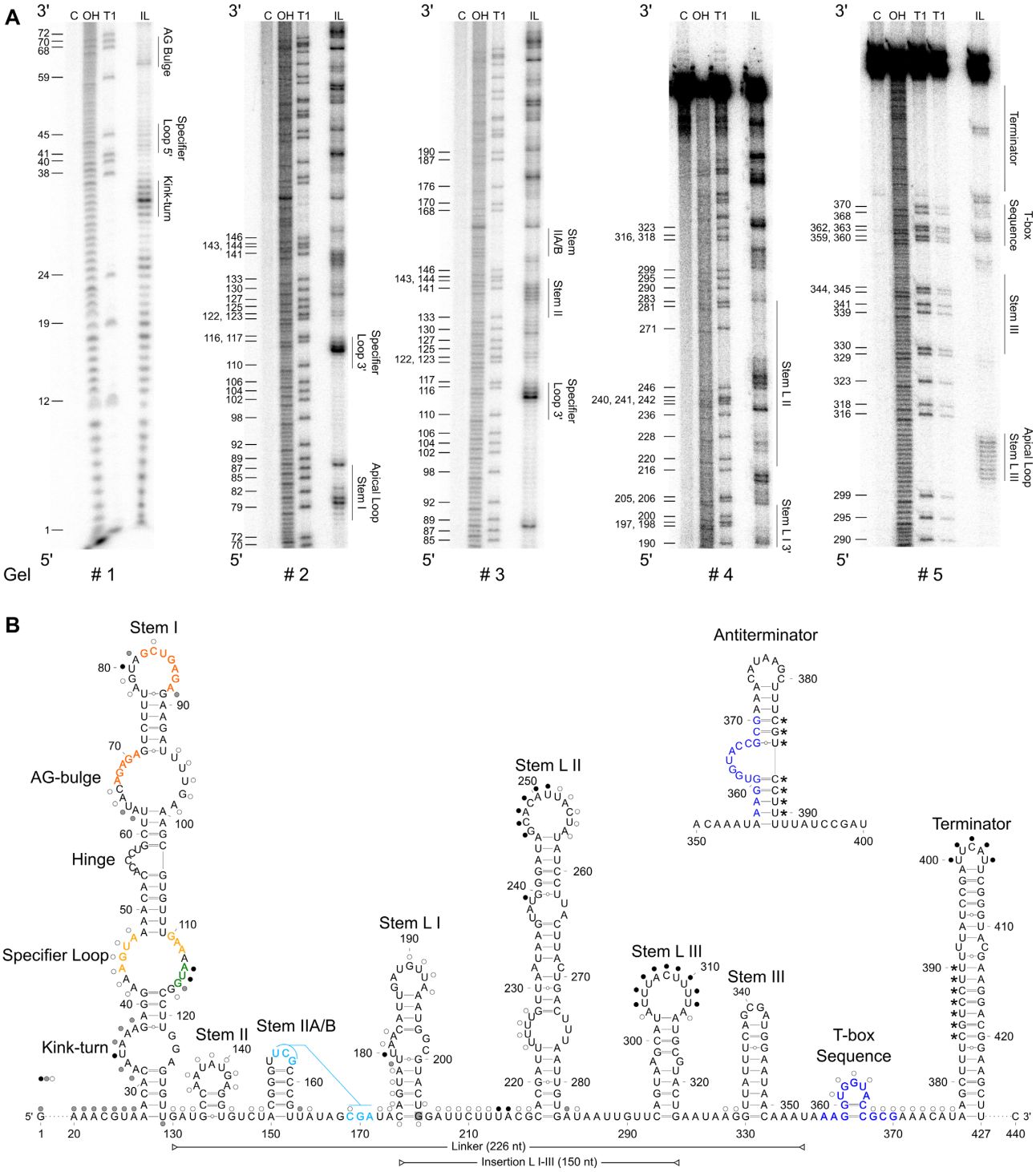

Figure 2. Secondary structure of *met* leader. (**A**) In-line probing PAA gels used to build 2D model. Nomenclature of structural motifs according to (9). Additional stems within linker region are numbered L I to L III. Position of guanosines (G) is given on the left of each gel. Structural motifs are specified on right side of each gel. C: control reaction; untreated RNA, OH: alkaline hydrolysis reaction; ladder, T1: RNase T1-treated RNA; G-specific ladder, IL: in-line reaction. (**B**) 2D structure model of *met* leader in its OFF state, predicted antiterminator 2D structure is shown above. Color of dots (black, gray, white) next to nucleotides indicates cleavage intensity (high, medium, low) detected in (A). Interacting nucleotides of specifier loop are shown in yellow, base pairing nucleotides of AG-bulge and apical loop of stem I in orange, specifier codon in green, potentially interacting nucleotides of stem IIA/B pseudoknot in light blue, T-box sequence in dark blue. Linker region between stem I and T-box sequence and insertion region of stem L I–III are indicated by horizontal bars. Nucleotides of terminator base pairing with T-box sequence in antiterminator conformation are marked by asterisks (*). G 205 highlighted in gray indicates 5′ end of short *met* leader RNA used for in-line probing.

nucleotides (nt 384–390, marked by asterisks in Figure 2B) that are capable to basepair with the T-box sequence to support antiterminator formation once the system is ON (Figure 2B, top). Thus, in presence of uncharged met-tRNA, the proximal 5′-part of the terminator stem and the T-box sequence become part of the antiterminator, thereby forming the characteristic T-box bulge (nt 361–367) which is prone to interact with the free 3′-CCA end of tRNA ligands (Figure 2B, top; Figure 1C).

met leader RNA cleavage

Endonucleolytic cleavage releases the met leader RNA from met operon mRNA. We previously reported that also under methionine-rich conditions basic transcription of the *met* leader takes place as a stand-alone transcript of 440 nucleotides in size resulting from Rho-independent transcription termination (Figure 3A, first lane). On the contrary, no transcription of the *met* operon occurs (Figure 3A, second lane and (6)). Upon methionine depletion, *met* leader transcription is usually further induced with transcriptional read-through into the downstream *met* operon (6). In these read-through transcripts, we actually expected the *met* leader RNA to be attached to the *met* operon mRNA, which would give rise to a long transcript of ∼7.6 kb in size. However, we were never able to detect stable transcripts of this size (6). Instead, Northern blot hybridization of total RNA with a *met* leader-specific probe using 1.2% agarose gels shows a band whose size (∼400 nt) corresponds to that of the *met* leader RNA alone (Figure 3A, third lane). Re-hybridization of the same blot with a probe from the 3′-end of the *met* operon mRNA (i.e. *metE*) detected two signals. The faint 7.2 kb band in Figure 3A (fourth lane) would match the size of the *met* operon mRNA without the *met* leader, suggesting release of the latter by endonucleolytic cleavage, while the strong 4 kb 3′ *met* operon signal is unexpectedly small (for reasons see paragraphs below) (Figure 3A). Rifampicin stability assays (using 5% PAA gels for higher resolution) identified two *met* leader-specific RNA species, a faint 440-nt band and a more abundant 390-nt fragment, which are both short-lived and become rapidly degraded (Figure 3B). To substantiate the hypothesis of *met* leader RNA cleavage and release, we performed 5′-RACE with a *metI*-specific primer and native total RNA to determine the 5′-end of *met* operon mRNA (see Materials and Methods for details). Successful PCR amplification of *met* operon-specific fragments by this approach confirmed that, upon methionine depletion, transcriptional read-through occurs from the *met* leader into the *met* operon (data not shown). Nucleotide sequencing of the amplicons revealed that the 5′-ends of 50% (n = 12) of *met* operon transcripts are located at position 418 in the 3′-portion of the *met* leader (Figure 3C and Supplementary Table S4). We conclude from this experiment that the read-through transcripts must have undergone endonucleolytic cleavage, as the 5′-RACE data were obtained with (RNA 5′ pyrophosphohydrolase, RppH) untreated total RNA, indicating presence of 5′ monophosphate ends which are typically generated upon RNA cleavage events in native RNA molecules. Cleavage of the transcript separates the *met* leader RNA from the *met* operon mRNA, thereby leaving the last 23 nt of the 3′- *met* leader end attached to the *met* operon mRNA (Figure 3C).

RNase III is involved in met leader RNA decay. As shown in Figure 3B, we found the *met* leader RNA species to be short-lived. In Gram-positive bacteria, main players of RNA decay are RNases III (a double-strand (ds)-specific endoribonuclease), J1/J2 (a bifunctional single-strand (ss)-specific endo- and 5′-3′ exoribonuclease) and Y (a ss-specific endoribonuclease), the latter known to be involved in riboswitch RNA turnover in *Bacillus subtilis* and *S. aureus* (35–37). To study the influence of staphylococcal RNase(s) on *met* leader stability, we subjected total RNA isolated from *S. aureus* conditional mutants of RNase J2 (*rnjB*::pMUTIN; '$rnjB_{\text{depleted}}$'), RNase III (*rnc*::pMUTIN; 'rnc_{depleted}') and a deletion mutant of RNase Y (*rny::ermC*; Δ*rny)* (all grown in CDM without methionine) to Northern blot hybridization using 5% PAA gels. Figure 4A confirms the detection of two *met* leader-specific fragments (∼440 and ∼390 nt) by this approach, with similar band patterns being displayed by the wildtype and the Δ*rny* as well as $rnjB_{\text{depleted}}$ mutants, indicating that neither RNase Y nor RNase J2 are involved in *met* leader RNA degradation. In the rnc_{depleted} mutant background, however, enrichment of the larger 440 nt fragment was detectable (Figure 4A). Rifampicin stability assays and half-life determination further revealed that stability of the 440 nt transcript increased in the rnc_{depleted} strain, resulting in longer half-life of the *met* leader RNA in comparison to the wildtype, while *met* leader RNA degradation remained unaffected in the Δ*rny* and $rnjB_{\text{depleted}}$ mutants (Figure 4B, C). A faint 390 nt band arising from cleavage of the stand-alone *met* leader transcript was still detectable in rnc_{depleted} (Figure 4A). This is explicable by the nature of the rnc_{depleted} strain as conditional mutant that still displays minimal residual RNase III activity. Indeed, when using a RNase III deletion mutant (kindly provided by Isabelle Caldelari), the cleaved form of the *met* leader is no longer traceable (Supplementary Figure S1). Together, the combined data suggest that RNase III, but not RNases Y or J2, is an important driver in *met* leader RNA decay.

RNase III has a cleavage site within the met leader. To analyze the nature and exact size of the ∼390 and ∼440 nt *met* leader-specific RNA fragments, we determined their 5′- and 3′-ends. For this purpose, we performed cRACE with RNA isolated from *S. aureus* wildtype and the rnc_{depleted} mutant grown under methionine-deprived conditions. In both strains, the 5′-end of the *met* leader mapped to identical positions (i.e. nt 404,416 of the *S. aureus* strain Newman genome; nt 1 in Supplementary Figure S2), demonstrating that wildtype and rnc_{depleted} mutant initiate transcription of the riboswitch at the same site. Determination of 3′-ends by this approach, however, elucidated major differences between wildtype and the rnc_{depleted} strain (Figure 4D). Thus, in the wildtype, 68% of transcripts ended at position 388 of the *met* leader which matches the size of the lower band detected in Figure 4A, while 5% of transcripts ended more downstream in a region between nt 425 and 440 (Figure 4D), corresponding to the upper band in Figure 4A. In contrast, in the rnc_{depleted} strain (which still displays

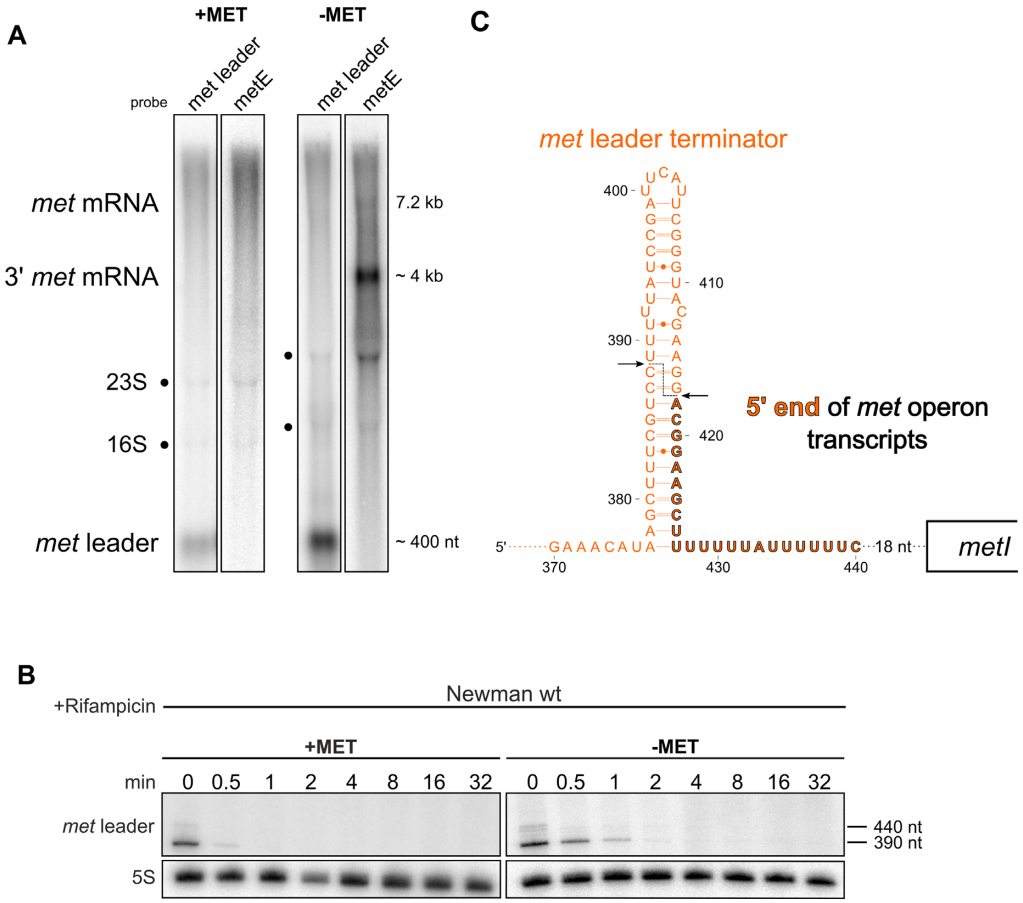

Figure 3. *met* leader is physically separated from *met* operon mRNA and rapidly degraded. (**A**) Total RNA isolated from *S. aureus* Newman grown in CDM with ('+MET') or without methionine ('−MET') was run on an agarose gel. Northern blot probed with a *met* leader-specific probe (lanes one and three) and re-probed with a *metE*-specific probe (lanes two and four). Positions of *met* leader RNA, *met* mRNA and 3′ region *met* mRNA are indicated on the left, approximate transcript sizes are given on the right. (**B**) Total RNA isolated from *S. aureus* Newman grown in CDM with ('+MET') and without methionine ('−MET') over a time course after rifampicin addition (0–32 min) was run on a PAA gel. Northern blot was hybridized with a *met* leader-specific probe and subsequently re-hybridized with a 5S rRNA-specific probe as loading control, transcript sizes are indicated on the right. (**C**) Schematic summary of *met* mRNA 5′ end determination by 5′ RACE. The scheme shows the very 3′ portion of the *met* leader with its terminator stem (marked in orange) and the beginning of *met* operon mRNA which is colored in black. Arrows mark the position of the *met* leader cleavage site identified within the terminator stem. Bold orange, black framed letters highlight the last 23 nucleotides of the *met* leader 3′-end that remain attached to *met* operon mRNA.

minor RNase III activity) only 30% of transcripts mapped to position 388, whereas 26% ended in the nt 425–440 region of the *met* leader (Figure 4D). Based on these results, we consider the lower (∼390 nt) *met* leader-specific RNA fragment to represent an RNase III-derived cleavage product of the *met* leader. The faint upper (∼440 nt) fragment, however, reflects non-cleaved *met* leader stand-alone RNA species which are likely to result from residual transcription termination events that continue to occur even upon activation of the system under methionine-deprived conditions. When combining these findings with the 5′-RACE data obtained for *met* operon mRNA 5′-end detection (see above), we conclude that cleavage occurs at positions 388 ^ 389 and 417 ^ 418 of the *met* leader RNA, generating a 2-nucleotide 3′ overhang that is typical for RNase III action (Figure 3C). According to the structural probing data, the identified cleavage site is located within the terminator stem of the riboswitch which is in good agreement with the function of RNase III as ds-specific endoribonuclease (Figure 2B).

RNase III targets the terminator stem structure of the met leader RNA. To further challenge the hypothesis of terminator cleavage by RNase III, we generated a series of markerless chromosomally encoded *S. aureus* mutants carrying alterations within the terminator/ antiterminator platform and studied the effects of these mutations on *met* leader RNA cleavage. In the first mutant, named Ter_mutated_1, we retained the terminator stem structure and the base-pairing strength, but altered the terminator nucleotide sequence (Figure 5A). The structure of the Ter_mutated_1 *met* leader RNA was assessed by in-line probing, confirming presence of a terminator stem similar to that of the wildtype (Figure 5B). Northern analysis of total RNA, isolated upon growth with and without methionine, demonstrates that *met* leader RNA cleavage is strongly impaired in mutant Ter_mutated_1, resulting in enrichment of non-cleaved 440 nt *met* leader RNA (Figure 5C). Next, we created mutants (i) Ter_destab in which introduction of mismatches prevented terminator stem formation (Figure 5A and B) as well as (ii) mutant ΔAntiTer&Ter in which the

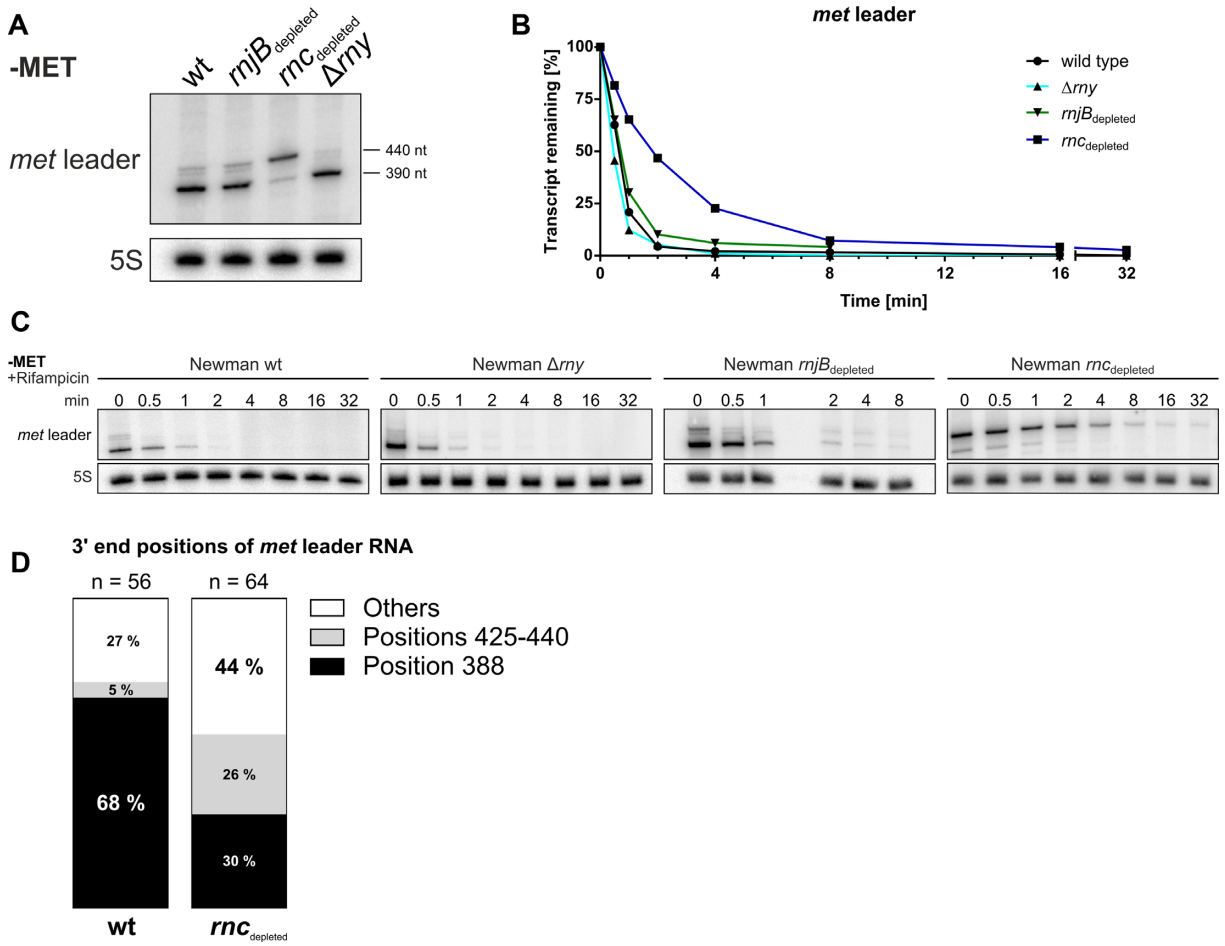

Figure 4. Influence of *S. aureus* RNases on *met* leader stability. (**A**) Total RNA isolated from *S. aureus* Newman and isogenic RNase J2 ($rnjB_{depleted}$), RNase III ($rnc_{depleted}$) and RNase Y (Δ*rny*) mutants grown in CDM without methionine ('−MET') was run on a PAA gel. Northern blot was hybridized with a *met* leader-specific probe and subsequently re-hybridized with a 5S rRNA-specific probe as loading control. Approximate transcript lengths are indicated on the right. (**B**) Quantification of *met* leader transcript levels over time calculated from rifampicin stability assays shown in (C). (**C**) Total RNA isolated from RNase mutant strains grown in CDM without methionine ('−MET') over a time course after rifampicin addition (0–8 and 0–32 min, respectively) was run on a PAA gel. Northern blot was hybridized with a *met* leader-specific probe and subsequently re-hybridized with a 5S rRNA-specific probe as loading control. (**D**) Graphical representation of cRACE data obtained for *met* leader transcript 3′ ends in the wild type 'wt' and the $rnc_{depleted}$ strain grown in CDM without methionine. Percentage of respective 3′ end positions of all analyzed transcripts are displayed in the respective column.

entire antiterminator and terminator sequence stretch (nt 352 to 439) was deleted. Although the *met* leader is transcribed (reflected by presence of multiple *met* leader RNA-specific bands), precise *met* leader RNA cleavage is completely abolished in both mutants (Figure 5C). Of note, no enrichment of non-cleaved stand-alone *met* leader RNA is detectable in mutants Ter_destab and ΔAntiTer&Ter which both lack the terminator stem structure (Figure 5C). Finally, when analyzing the mutants for *met* operon transcription (using a *metE*-specific probe), mutant Ter_mutated_1 was unable to switch on downstream gene transcription under methionine-deprived conditions, which is consistent with an impaired T-box function in this mutant (Figure 5D). In mutants Ter_destab and ΔAntiTer&Ter, however, *met* operon transcription was found to be activated independent of methionine supply, reflecting deregulation of the transcription control mechanism due to the lack of an effective transcription termination signal. From the combined data we conclude that the terminator stem is a necessary structure for *met* leader RNA degradation which, however, also involves sequence specificity to initiate physical separation of the *met* leader from *met* operon mRNA.

Sequence constraints of met leader RNA terminator cleavage. RNase III is known to target RNA helices of 20–25 bp in size, with the homodimeric enzyme usually cleaving within a GC-rich sequence motif thereby generating 3′-overhangs of two nucleotides on the processed dsRNA products (38). Previous *in vitro* studies demonstrated that the sequence of the cleavage site itself is not required for recognition by RNase III and its catalytic activity (39). Instead, nucleotides outside the cleavage site, designated as proximal, middle and distal protein-interacting boxes, were shown to be required for substrate recognition and cleavage (Figure 5A) (40). As shown in Figures 3–5, cleavage of the *met* leader occurs between nucleotides 388 ^ 389 and 417 ^ 418, respectively. To analyze putative sequence-specific constraints for RNase III action on the *met* leader *in vivo*, three *met* leader mutants (mutants Ter_mutated_2, 3 and 4) with point mutations within or adjacent to the cleavage site were gen-

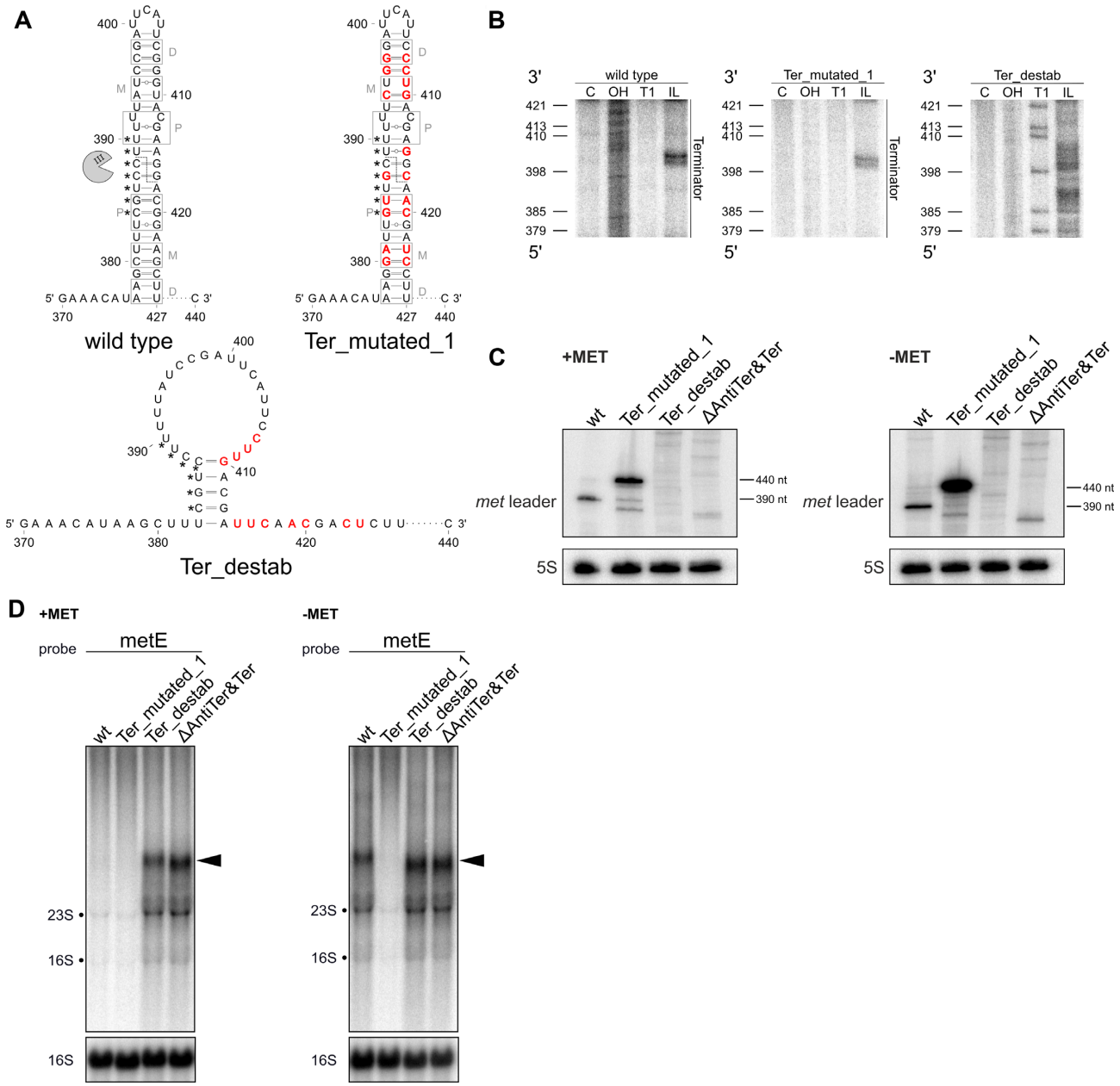

Figure 5. Alteration of the terminator stem structure and influence on *met* leader cleavage. (**A**) Predicted secondary structures of terminator regions in *met* leader RNAs of wild type and mutants 'Ter_mutated_1' and 'Ter_destab'. Point mutations introduced are highlighted in red, gray boxes indicate regions interacting with RNase III dimers as described in (40), P: proximal, M: middle, D: distal box. Nucleotides engaged to form the T-box bulge in antiterminator conformation (see also Figure 2B) are marked by asterisks (*). RNase III is depicted as pac-man. Position of RNase III cleavage site in wild type *met* leader is indicated by a dashed line. (**B**) In-line probing gel sections of the terminator region of *met* leader wild type, 'Ter_mutated_1' and 'Ter_destab' RNA are shown. Position of guanosines (G) as in 'Ter_destab' is given on the left of each gel, annotations as in Figure 2A. (**C**) Total RNA isolated from *S. aureus* Newman and the *met* leader mutants 'Ter_mutated_1', 'Ter_destab' and 'ΔAntiTer&Ter' grown in CDM with ('+MET') or without methionine ('−MET') was run on a PAA gel. Northern blot was hybridized with a *met* leader-specific probe and subsequently re-hybridized with a 5S rRNA-specific probe as loading control. (**D**) Total RNA same as in (C) was run on an agarose gel. Northern blot was probed with *metE*-specific probe and subsequently re-hybridized with a 16S rRNA-specific probe as loading control. Black arrowheads mark 3′ *met* mRNA transcripts.

erated (Figure 6A). Structural probing confirmed integrity of the terminator stem structure (Figure 6B) and Northern analyses demonstrate that *met* leader RNA cleavage is still detectable in all three mutants (Figure 6C). However, in mutant Ter_mutated_3 (which carries three nucleotide exchanges), enrichment of non-cleaved *met* leader stand-alone RNA species occurs, suggesting that RNase III-mediated cleavage is diminished, but not completely abolished in this mutant (Figure 6C). The data corroborate that the sequence of the cleavage site itself is of minor importance for endonucleolytic processing by RNase III *in vivo*. Nevertheless, certain critical sequence constraints adjacent to the cleavage site seem to exist which influence activity of the enzyme.

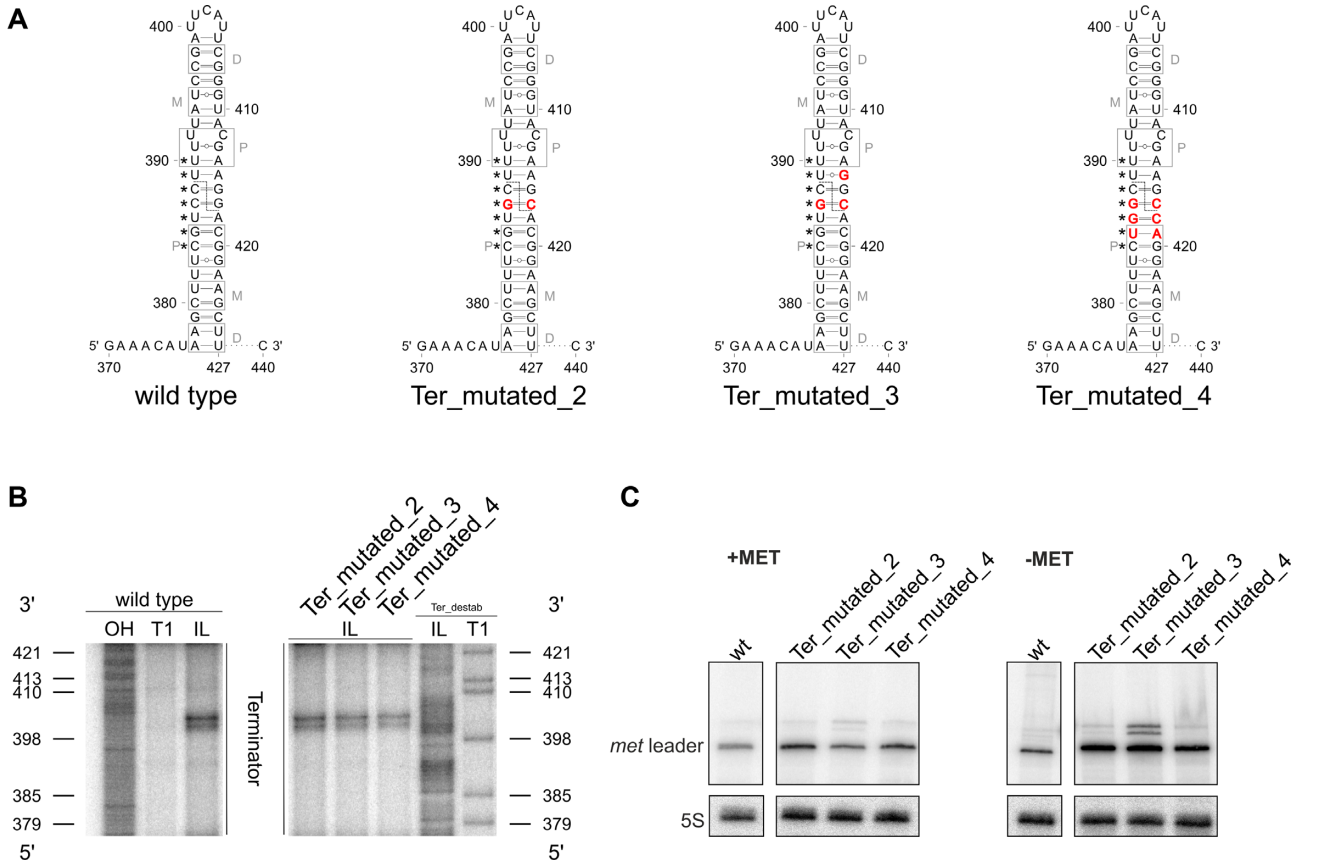

Figure 6. Sequence constraints of *met* leader RNA terminator cleavage. (**A**) Sequence and predicted secondary structure of terminator regions in *met* leader RNAs of wild type and mutants 'Ter_mutated_2', 'Ter_mutated_3' and 'Ter_mutated_4'. Point mutations introduced are highlighted in red, gray boxes indicate regions interacting with RNase III dimers as described in (40), P: proximal, M: middle, D: distal box. Nucleotides engaged to form the T-box bulge in antiterminator conformation (see also Figure 2B) are marked by asterisks (*). Position of RNase III cleavage site in wild type *met* leader is indicated by a dashed line. (**B**) In-line probing gel sections of the terminator region of *met* leader wild type, 'Ter_mutated_2', 'Ter_mutated_3' and 'Ter_mutated_4' RNA are shown. Position of guanosines (G) as in 'Ter_destab' is given on the left and right of the gel, respectively, annotations as in Figure 2A. (**C**) Total RNA isolated from *S. aureus* Newman and the *met* leader mutants 'Ter_mutated_2', 'Ter_mutated_3' and 'Ter_mutated_4' grown in CDM with ('+MET') or without methionine ('−MET') was run on a PAA gel. Northern blot was hybridized with a *met* leader-specific probe and subsequently re-hybridized with a 5S rRNA-specific probe as loading control.

Fate of *met* operon (*metICFE-mdh*) mRNA and protein accumulation

Stability of the metICFE-mdh mRNA varies over the length of the transcript. Highly structured 5′ UTRs (such as riboswitches) usually protect mRNAs from degradation. The data obtained so far demonstrate that the *met* operon mRNA exists as a transcript that lacks the riboswitch (after *met* leader RNA cleavage) and which may undergo RNA decay. To study the stability of the *met* operon mRNA we performed rifampicin stability assays over the entire length of the transcript by using specific probes that target the single genes of the operon (Figure 7A–C). Figure 7B revealed that hybridization with a *metI*-specific probe, located in the 5′ portion of the transcript, resulted rather in a smear than a clear band. Only at time point t0 (prior to rifampicin addition), a blurry *metI*-specific band of 1 kb in size was detectable which, however, was highly instable as it was found to be degraded already 0.5 min after transcription arrest by rifampicin. Hybridization with a *metC*-specific probe, located in the 5′ portion of the transcript as well, did not result in any detectable signal (neither smear nor band). In contrast, hybridization with *metE*- and *mdh*-specific probes from the 3′-end of the operon revealed a fragment of ∼4 kb in size (Figure 7B). Compared to *metI*, this *metE*/ *mdh*-specific fragment was more stable as it was still detectable four minutes after rifampicin-induced transcription arrest (Figure 7B). The results of these experiments demonstrate that the stability of the *metICFE-mdh* mRNA varies over the length of the transcript with the 5′-portion being more instable than the 3′ part of the operon.

The stable 3′-part of the met operon mRNA covers partly metF as well as the complete metE and mdh genes. Next, we further characterized the length and nature of the stable 4 kb *metE*/ *mdh*-specific fragment. Northern blot hybridization with various probes revealed that the stable transcript comprises the 3′ portion of *metF* as well as the *metE* and *mdh* genes (Figure 7C and B). Size calculation and Northern blot hybridization with a 5′-*metF* probe (data not shown) suggested that *metF* is only partly covered by the stable 4 kb transcript. Indeed, 5′-RACE experiments mapped the majority of the 5′-ends of the transcript to the 3′ portion

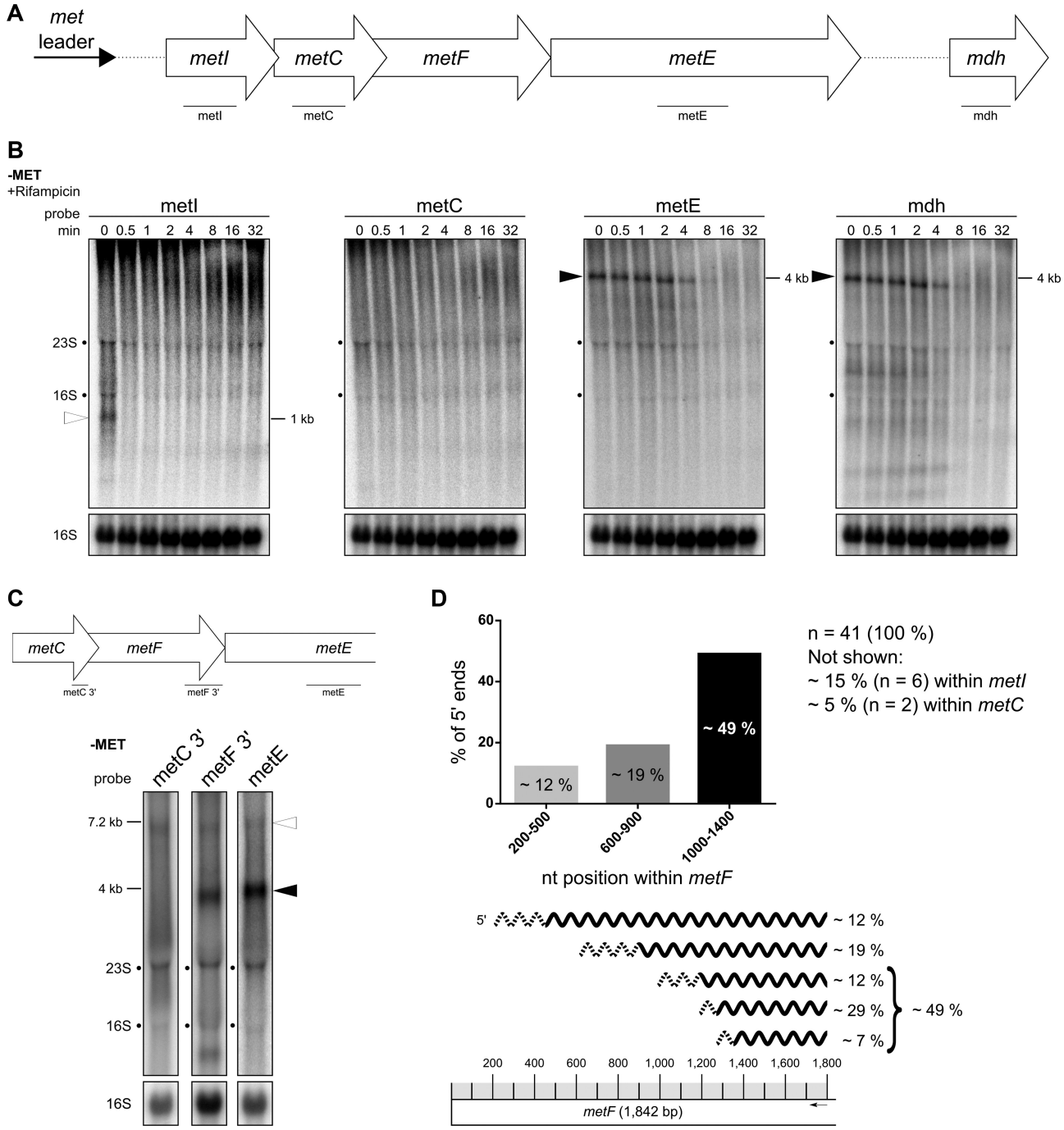

Figure 7. Stability of the *met* operon mRNA varies over length of the transcript. (**A**) Schematic view of the organization of the *met* operon including its 5′ UTR (*met* leader). Lines below gene arrows indicate relative positions of the respective probes used in (B). (**B**) Total RNA isolated from *S. aureus* Newman grown in CDM without methionine ('−MET') over a time course after rifampicin addition (0–32 min) was run on an agarose gel. Northern blot was probed for *metI*, *metC*, *metE* and *mdh*. Open arrowhead marks *metI* mRNA and black arrowheads mark 3′ *met* mRNA. Approximate transcript lengths are indicated on the right of the respective blot. Re-hybridization with a 16S rRNA-specific probe was used as loading control. (**C**) Schematic view of the *met* operon 3′ region (without *mdh*) and relative positions of probes used. Total RNA isolated from *S. aureus* Newman grown in CDM without methionine ('−MET') was run on an agarose gel. Northern blot was probed for 3′ region of *metC* ('metC 3′'), 3′ region of *metF* ('metF 3′') and *metE*. Open arrowhead marks full-length *met* operon mRNA (without *met* leader) and black arrowhead marks 3′ *met* operon mRNA. Approximate transcript lengths are indicated on the left. Re-hybridization with a 16S rRNA-specific probe was used as loading control. (**D**) Summary of 5′-RACE data. Upper diagram: Percentage of 5′ ends detected within distinct regions of *metF*. Lower part: Mapping of the detected 5′ ends to the *metF* region. Scale of the *metF* gene is illustrated at the bottom. Gray boxes represent 100 nucleotides each and the black arrow marks the approximate position of the primer used for cDNA synthesis. Transcripts characterized by 5′-RACE are depicted as wavy lines, dashed regions symbolize the range of detected 5′ ends. The percentage of each transcript group detected is given on the right.

of *metF* (Figure 7D). As shown in Figure 7D, the 5′ ends span a wide range within *metF* which speaks against the presence of a dedicated endoribonucleolytic cleavage site in this region. Finally, by performing cRACE experiments, we found the 3′ end of the stable 4 kb transcript to map 81 nucleotides downstream of the *mdh* stop codon, demonstrating presence of a 3′-UTR in *met* operon mRNA (data not shown). Together, the stable part of the *met* operon mRNA spans a region between the 3′-*metF, metE* and *mdh* genes as well as an 81 nt-long 3′-UTR.

RNase J is involved in metICFE-mdh mRNA decay. Next, we were interested in identifying the RNase(s) involved in the exonucleolytic degradation of the cleaved *met* operon mRNA from the 5′ end. The sole enzyme with known 5′ to 3′ exonuclease activity in *S. aureus* is RNase J (J1/J2). Although the J1/J2 enzyme complex is not essential in *S. aureus*, generation of J1 and J1/J2 double mutants by classical temperature-sensitive allele replacement vectors was notoriously difficult due to growth impairment of J1 mutants at 42°C (22). Eventually, employing a novel temperature-independent replacement vector allowed mutation of the RNase J-encoding genes in a dedicated pyrimidine auxotrophic *S. aureus* background (i.e. strain *S. aureus* PR01) (22). For assessing the influence of RNase J on *met* operon mRNA decay, we employed RNase J1 (Δ*rnjA*), J2 (Δ*rnjB*) and J1/J2 (Δ*rnjA/B*) mutants obtained in *S. aureus* PR01 (all kindly provided by Peter Redder). Initial experiments, however, revealed that *S. aureus* PR01 (for unknown reasons) is unable to activate its own chromosomal *met* operon upon methionine deprivation, making it impossible to study *met* leader/ *met* operon decay directly in the PR01 mutant strains (data not shown). We therefore cloned the *met* leader (under the control of its native promoter) along with the adjacent 5′-region of *metI* onto a vector which was transformed into *S. aureus* PR01 wildtype as well as into the three isogenic RNase J mutants (Figure 8A). Figure 8B demonstrates that methionine deprivation indeed induces *met* leader/ *metI* transcription from the vector (though only at low level). In the *S. aureus* PR01 wildtype background plasmid-derived *metI*-specific mRNA is not detectable which is probably due to its rapid degradation (Figure 8B). In contrast, the *metI*-specific transcript is enriched in the RNase J1 (Δ*rnjA*), J2 (Δ*rnjB*) and J1/J2 (Δ*rnjA/B*) mutants (Figure 8B). These data strongly suggest that the RNase J1/J2 complex is involved in the degradation of *met* operon mRNA by executing 5′ to 3′ exonucleolytic cleavage of the RNA.

Cleavage by RNase III facilitates met operon mRNA degradation. Next, we asked the question whether or not RNase III-mediated release of the *met* leader might have an influence on degradation of the *met* operon mRNA from the 5′-end. As detection of full-length *met* operon transcripts proved to be notoriously difficult (Figures 3 and 7), we focused on the stability of the very 5′-end of the *met* operon mRNA and transformed the *met* leader/ 5′ *metI* plasmid (described above) into *S. aureus* Newman and its isogenic RNase III (*rnc*::pMUTIN; $rnc_{depleted}$) mutant. Northern hybridization using a 5′ *metI*-specific probe (Figure 9A) resulted in the detection of a larger (i.e. 970 nt) fragment in the $rnc_{depleted}$ mutant in comparison to the 550-nt band present in the wildtype (Figure 9B). The fragment size in the $rnc_{depleted}$ strain is in agreement with a non-cleaved plasmid-derived *met* leader/ 5′ *metI* transcript, confirming lack of *met* leader RNA release in a $rnc_{depleted}$ background (Figure 9B). Importantly, the non-cleaved *met* leader/5′ *metI* transcript becomes stabilized in the $rnc_{depleted}$ strain. Thus, rifampicin stability assays revealed that, in the RNase III-proficient wildtype, processed 5′ *metI* RNA is degraded after two minutes, while in the $rnc_{depleted}$ background the non-cleaved *met* leader/5′ *metI* transcript is still detectable after eight minutes (Figure 9C). These data led us to conclude that the *met* leader protects *met* operon mRNA from 5′ to 3′ exonucleolytic degradation. Cutting off the *met* leader through RNase III, however, abolishes this effect and favors degradation of the *met* operon mRNA.

Detection of met operon-encoded proteins. Next, we asked the question of whether mRNA stability might influence protein amounts or synthesis rates. Thus, we initially determined intracellular proportions of *met* operon-encoded MetI, MetC, MetF, MetE and Mdh enzymes by liquid chromatography (LC)/mass spectrometry (MS) (Figure 10A). Relative protein quantification by LC–MS/MS analysis, performed in mid-exponential growth phase, identified MetE as the most abundant protein of the *met* operon-encoded enzymes (69%), followed by Mdh (11%) and MetC (10%). The least abundant proteins were MetF (4%) and MetI (6%) (Figure 10A). As detectable cellular protein levels are the result of available transcript amounts, translation rate and protein degradation, we studied these processes as well. First, we analyzed protein stabilities by measuring the half-lives of the Met enzymes. For this purpose, we performed a pulse experiment by combining stable isotope labeling of amino acids (SILAC) with gel-free LC–MS/MS analysis (41). The SILAC approach allows to differentiate between 'old' and 'newly' synthesized proteins according to their respective isotope labels which are acquired upon a shift to media containing either stable isotope labeled (heavy) or unlabeled (light) amino acids (Figure 10B). In brief, following growth in CDM (without methionine, but containing light arginine and lysine) to mid-exponential phase, bacteria were washed with PBS to remove any light amino acids and shifted to CDM containing heavy arginine and lysine (label switch) (Figure 10B). Samples were taken at different time points after the label switch (t0′, t15′, t30′, t60′ and t240′) and analyzed by LC–MS/MS (Figure 10B, C). The label switch set a defined end-point of protein synthesis with light amino acids. Accordingly, proteins synthesized after the label switch exclusively contain heavy arginine and lysine residues. Hence, the label switch allows monitoring the stability of light proteins accumulated prior to the label switch thereby distinguishing them from newly synthesized heavy proteins. As this approach only considers proteins made prior to the switch, changes in transcription and translation that might occur after the switch, will not influence the results of the half-life determinations. The experiment revealed that, in contrast to its low abundance, MetI displayed a striking long half-life of 7.2 h (Figure 10C). Also Mdh, which exhibits a half-life of 8.2 h, is long-lived, while stability of MetE is lower (half-life 4.8 h). Finally, the

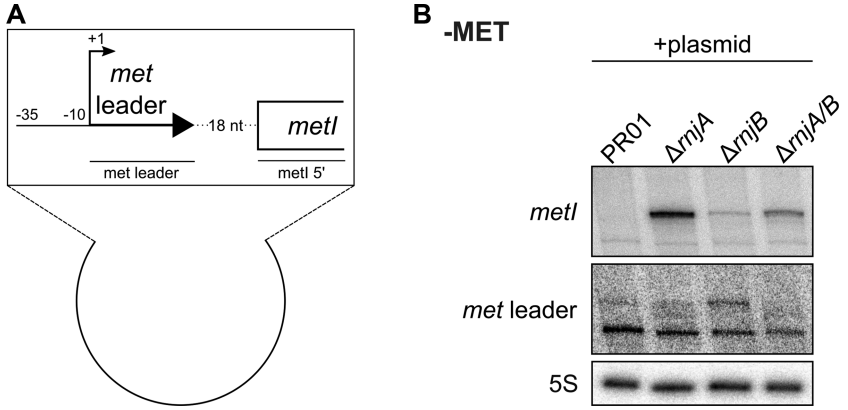

Figure 8. RNase J is involved in *met* operon mRNA degradation. (**A**) Scheme of the plasmid transformed into *S. aureus* SA564RD Δ*pyrFE* ('PR01') and its isogenic RNase J1 ('Δ*rnjA*'), RNase J2 ('Δ*rnjB*') and RNase J1/J2 double ('Δ*rnjA/B*') mutants. '–35' and '–10' indicates the promoter region. Arrow with +1 marks the transcription start site of *met* leader. The *met* leader sequence is depicted as thick, black arrow. First 215 nt of *metI* are shown as open rectangle. Lines below genes indicate relative positions of probes used in (B). (**B**) Total RNA was isolated from *S. aureus* SA564RD Δ*pyrFE* ('PR01') and its isogenic RNase J1 ('Δ*rnjA*'), RNase J2 ('Δ*rnjB*') and RNase J1/J2 double ('Δ*rnjA/B*') mutants. Bacteria were grown in MH medium to OD 0.5. Then cultures were washed twice with PBS, bacteria were shifted into CDM without methionine ('−MET') supplemented with pyrimidine for 30 min and samples were taken. 5 μg of total RNA was run on a PAA gel. Northern blot was hybridized with a *met* leader-specific probe, re-probed with a *metI* 5′-specific probe and subsequently re-hybridized with a 5S rRNA-specific probe as loading control.

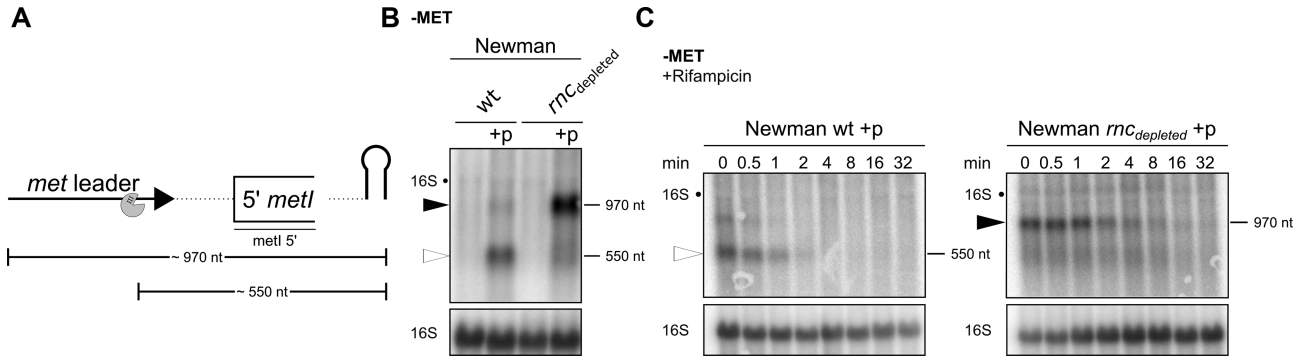

Figure 9. RNase III cleavage of terminator stem facilitates 5′ *met* operon mRNA exonucleolytic degradation. (**A**) Scheme of transcripts detected in (B); *met* leader sequence depicted as thick, black arrow, first 215 nt of *metI* shown as open rectangle, plasmid-derived transcription terminator shown as hairpin. Line below *metI* indicates relative position of the probe used in (B) and (C). RNase III cleavage site is shown as pac-man. Approximate transcript sizes are given below the scheme. (**B**) Total RNA was isolated from *S. aureus* Newman, its isogenic RNase III ($rnc_{depleted}$) mutant and from both strains transformed with the plasmid ('+p') detailed in Figure 8A grown in CDM without methionine ('−MET'). RNA was run on an agarose gel. Northern blot was probed with a *metI* 5′-specific probe. Open arrowhead marks ∼550 nt transcript and black arrowhead marks ∼970 nt transcript. Approximate transcript lengths are indicated on the right of the blot. Re-hybridization with a 16S rRNA-specific probe was used as loading control. (**C**) Total RNA was isolated from *S. aureus* Newman and its isogenic RNase III ($rnc_{depleted}$) mutant strain transformed with the plasmid ('+p') grown in CDM without methionine ('−MET') over a time course after rifampicin addition (0–32 min). RNA was run on an agarose gel. Hybridization and labelling as described for (B).

lowest half-life in this experiment was displayed by MetC (i.e. 2.2 h) (Figure 10C). To investigate a putative direct influence of *met* operon mRNA stability on protein synthesis, we next determined the synthesis rates of the Met enzymes. Thus, we again performed a SILAC experiment, but now adding rifampicin to block further *met* operon transcription after the label switch (Figure 10B). In this experimental set up, Met enzymes will be exclusively translated from transcripts made prior to transcription arrest, with mRNA stability likely to influence protein synthesis rates. As described above, accumulation of these newly synthesized proteins can be readily monitored by measuring the incorporation of heavy arginine and lysine residues after the label switch (Figure 10B). Samples were taken before and after rifampicin addition at different time points after the label switch and analyzed by LC–MS/MS (t0′ and t30′) and Northern hybridization (t0′, t15′ and t30′) (Figure 10B&D). The latter confirmed immediate *met* operon transcription arrest after the addition of rifampicin as only traces of the stable *metE*-specific *met* operon mRNA were detectable after 15 min (Figure 10D, right). From the LC–MS/MS data we calculated the doubling times of the enzymes as a measure for the protein synthesis rates (Figure 10D, left). Among all Met enzymes, MetE and Mdh displayed the shortest doubling time (i.e.∼30 min), reflecting a high protein synthesis rate. Higher doubling times (and accordingly lower protein synthesis rates) were recorded for MetI and MetC (∼70 min) as well as for MetF (150 min) which displayed the lowest synthesis rate (Figure 10D, left). As these data are commensurate to *met* operon transcript stabilities, we conclude that varying mRNA degradation affects translation and the resulting protein amounts, with the

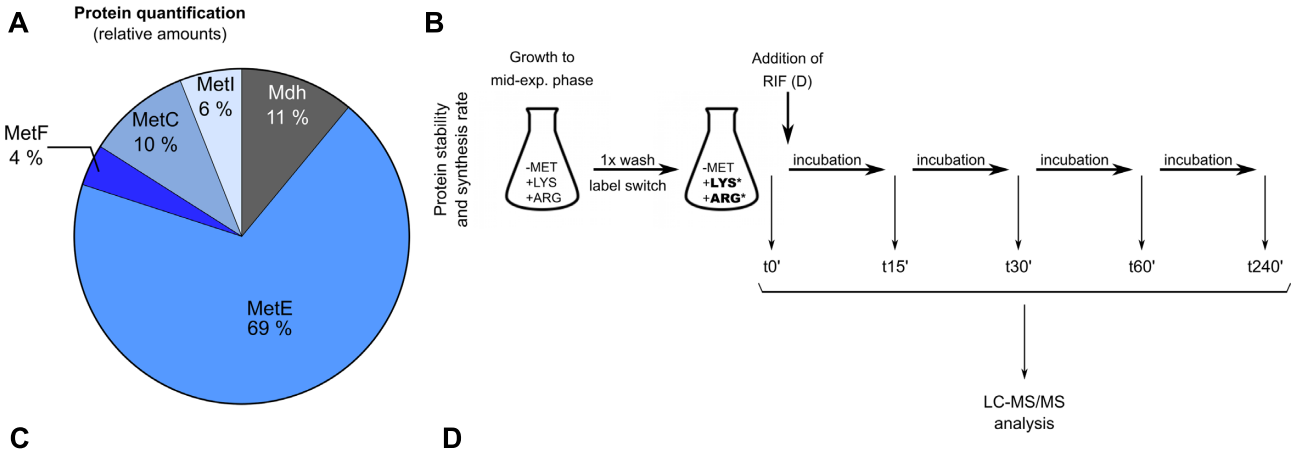

C

Protein stability

Deduced from time course of unlabeled proteins, representing proteins synthesized prior to label switch.

Protein name	Half-life [h]
MetI	7.2
MetC	2.2
MetF	n.d.
MetE	4.8
Mdh	8.2

D

Protein synthesis rate

Deduced from time course of heavy proteins, representing proteins synthesized after label switch and transcription arrest.

Protein name	Doubling time [min]
MetI	72
MetC	68
MetF	150
MetE	33
Mdh	34

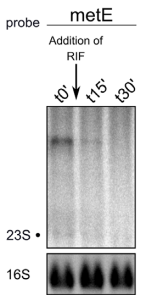

Figure 10. Detection of *met* operon-encoded proteins by proteomics. (**A**) Relative cellular protein amounts of *met* operon-encoded enzymes as detected by LC–MS/MS analysis. (**B**) Experimental design for protein stability (**C**) and protein synthesis rate (**D**) determinations. Asterisks (*) indicate the heavy amino acids lysine and arginine added upon label switch (see text for details). (**C**) Half-lives of *met* operon enzymes as calculated from LC-MS/MS data of unlabeled proteins. t0′, t15′, t30′, t60′ and t240′ samples were used for half-life determination. (**D**) Synthesis rates of *met* operon enzymes after transcription arrest by addition of rifampicin (RIF) as calculated from LC–MS/MS data of heavy proteins. t0′ and t30′ samples were used for determination of doubling time. Corresponding total RNA was run on an agarose gel. Northern blot was probed with *metE*-specific probe. Arrow marks addition of rifampicin. 16S rRNA detected in Midorigreen-stained gel is shown as loading control. (h), hours; (min) minutes; n.d., not determined.

latter being further influenced by variations in protein stability and possibly other (so far) unknown factors.

DISCUSSION

met leader RNA secondary structure

Secondary structure determination revealed that the *met* leader RNA indeed harbors all structural features known from classical T-box riboswitches. By its size, however, the element stands out from the majority of other T-box riboswitches, including those with methionyl-tRNA specificity (2,42). Interestingly, the *met* leader RNA T-box riboswitch was previously shown to prefer interaction with initiator-methionyl-tRNA over elongator-methionyl-tRNA to activate the system (6). As both methionyl-tRNA species possess a CAU anticodon to be recognized by the specifier AUG codon, discrimination is likely to involve additional structural features both on the tRNA and *met* leader RNA side. tRNA structures usually recognized by T-box-riboswitches comprise, in addition to the anticodon and the 3′ CCA sequence, the T- and D-arms which form the tRNA elbow in canonical L-shaped tRNAs (10). Sequence-specific differences between initiator- and elongator methionyl-tRNAs mainly exist in the D- and T-arms as well as in the acceptor stems of these tRNA species. Co-crystallization and NMR studies with *glyQS* and *tyrS* T-box riboswitches demonstrate that the tRNA elbow and anticodon stem closely interact with stem I of the T-box riboswitch (10,43–46). In this dynamic interaction, the kink-turn and hinge regions confer flexibility to stem I to enable bending over the tRNA (10,11,47). Except for the missing GA motif within the kink-turn, stem I of the *met* leader is not particularly different from other T-box riboswitches, suggesting similar structural interaction with methionyl-tRNAs, but making it unlikely that stem I considerably contributes to initiator/ elongator tRNA discrimination. The role of the adjacent stem II and stem IIA/B pseudoknot in T-box riboswitch function is still poorly understood, the more so as the structures may even lack in some systems (i.e. in *glyQS*) (9). Recent findings suggest that stem II bridges and latches the otherwise weak AU-rich specifier codon–tRNA anticodon interactions, making it dispensable for the GC-rich *glyQS* riboswitch codons (48). This lateral stabilization of the codon–anticodon interaction turned out to be essential in T-box riboswitches of the ultrashort stem I type, such as the *ileS* T-box riboswitch of *Mycobacterium smegmatis,* compensating for the absence of the stem I platform usually interacting with the tRNA elbow (49–51). It is therefore tempting to speculate that the short stem II of the *met* leader might be involved in the tRNA binding process as well. At least for the *glyQS* system, the linker region between stem I and stem III was suggested to play

a role in exact tRNA positioning by acting as a ruler to monitor the tRNA length and overall shape (52,53). Interestingly, the additional stem-loops within the linker region seem to be specific for the staphylococcal MET-T-box riboswitch, and it is well conceivable that they may play a role in methionyl-tRNA interaction and discrimination. Species-specific structural features contributing to differential tRNA selectivity have been previously described for the *S. aureus glyS* T-box riboswitch, suggesting certain evolutionary flexibility in T-box systems which might allow for adaptation to distinct metabolic profiles of bacteria (54). Finally, through the insertion of stems LI to LIII into the linker region, the *met* leader becomes unusually long. In concert with the specific structural features of the linker, it is possible that the extended transcription time to synthesize the long *met* leader might further facilitate correct recognition and positioning of the tRNA. Recent single-molecule fluorescence resonance energy transfer (smFRET) studies dissected tRNA/ T-box riboswitch interaction as a highly dynamic process that proceeds in two steps, with the anticodon being recognized first, followed by 3′-CCA binding through the T-box bulge (11). The latter step is accompanied by a conformational change of the distal part of the T-box riboswitch to contact the tRNA (11). Postulating that tRNA binding is an induced-fit process that takes place while the T-box riboswitch RNA is transcribed (55), extended transcription time of the *met* leader may allow for exact shape recognition and binding of the cognate tRNA. However, in absence of three-dimensional stuctural data of the *met* leader RNA (or any other MET-T-box riboswitch) this is mere speculation at the moment. In general, T-box riboswitches are increasingly recognized as promising targets for anti-infective drugs to interfere with bacterial growth (56–59). In that sense and in the light of the ongoing antibiotic resistance crisis, detailed structural analyses of bacterial T-box riboswitches is certainly a worthwhile task.

RNase III mediates *met* leader RNA cleavage

Apart from the long linker region, the most striking structural feature of the *met* leader RNA was the identification of a terminator stem that represents a target for cleavage by RNase III (Figures 2B, 4A). This is rather unusual as bacterial riboswitch turnover is commonly associated with the action of RNase P and RNase Y (36,37,60). The *met* leader terminator stem comprises a helix of 23 bp which is above the average length of terminator stems usually present in other T-box riboswitches (including MET-T-box systems) (2,42). RNase III requires double-stranded RNA stretches of 20–25 bp for cleavage, and it is therefore reasonable to suggest that the length of the stem in combination with presence of a GC-rich region renders the terminator an RNase III target (38,39). Lack of *met* leader RNA cleavage in mutants that are devoid of the terminator stem structure (Ter_destab, ΔAntiTer&Ter) or possessing a terminator stem with an altered sequence (Ter_mutated_1) (Figure 5C) strongly support this hypothesis. In agreement with our previous studies, *met* leader RNA was overabundantly present also under methionine-rich conditions in which the system is actually OFF. Indeed, in presence of methionine no *met* operon expression took place while constitutive basic transcription of the *met* leader occurred regularly under all growth conditions. This is attributed to the somewhat 'leaky' CodY-mediated repression of the system which most likely supports immediate activation of *met* operon transcription when needed. As the prematurely terminated *met* leader RNAs ('stand-alone transcripts') carry the terminator stem, RNase III-driven cleavage and decay of the *met* leader under methionine-rich conditions comes as no surprise (Figures 3 and 5). However, *met* leader RNA cleavage was also detected under methionine-deprived conditions when *met* operon mRNA was transcribed upon antiterminator formation and read-through into downstream *met* operon genes (Figures 3–6). As antiterminator and terminator are mutually exclusive structures, read-through transcripts should actually lack the terminator stem as RNase III target. However, our combined experiments clearly speak in favor of terminator stem presence and RNase III-mediated cleavage of the read-through transcripts. Terminator stem presence in read-through transcripts might be explained by the high thermodynamic stability of the terminator stem (free energy $\Delta G = -32.60$ kcal/mol) which is associated with its length and GC-richness (Figure 2B). Formation of the antiterminator is likely to be transient as it is the thermodynamically much weaker structure which is only required to allow the RNA polymerase to pass the distal expression platform of the T-box riboswitch to accomplish downstream gene transcription (8). At the same time, immediate terminator stem formation in read-through transcripts will release uncharged tRNAs from the T-box riboswitch which will then be available for amino acid charging, once sufficient amounts of the cognate amino acid is synthesized (8). In this respect, terminator stem formation in *met* leader/ *met* operon read-through transcripts makes sense.

RNase J mediates *met* operon mRNA decay

Cleavage of a (T-box) riboswitch by RNase III was a rather unexpected finding of this study. Commonly, riboswitch RNAs either remain attached to the mRNA or were shown to be cleaved by RNase P or RNase Y (36,37,60). In *B. subtilis thrS*, T-box riboswitch cleavage was found to occur immediately upstream of the terminator stem, leaving the structure as a protective element that stabilizes the mRNA and prevents degradation (61). In contrast, in the *S. aureus met* leader/*met* operon system we found the terminator stem to recruit RNase III to cleave off the *met* leader from the *met* operon mRNA, thereby considerably destabilizing the transcript (Figures 4 and 9). The data further show that *met* operon mRNA degradation occurs from the 5′-end (Figure 7), with the mRNA decay being accomplished by RNase J (Figure 8), the sole enzyme known to date in Gram-positive bacteria with 5′ to 3′ exoribonucleolytic activity (35). The RNase III cleavage removes the protective stem structure from the *met* mRNA and creates a 5′ monophosphate end that is prone to exonucleolytic degradation. Unexpectedly, mRNA degradation was not equally efficient over the length of the *metICFE-mdh* mRNA. Thus, the 5′ part of the transcript (encoding *metI, metC* and the 5′ part of *metF*) was more rapidly degraded than the 3′ end (covering the *metF* 3′, *metE* and *mdh* genes) (Fig-

ure 7). The molecular background of these differences in *metICFE-mdh* mRNA stability is currently not known. The scenario, however, is reminiscent of previous findings in *E. coli* and other bacteria showing that polycistronic mRNA can undergo differential RNA decay, leaving some genes within the operon more stable than others, with direct consequences for protein expression levels (62–65). In this respect, RNA decay was found to be regulated by mRNA secondary structures (62), and a recent study in *S. aureus* also identified distinct structural elements within a staphylococcal mRNA which influenced activity of RNase Y (66). It is well conceivable that similar functional elements might exist in the *metICFE-mdh* mRNA. However, preliminary bioinformatic analysis of the transcript did not reveal sufficient indications for that so far (data not shown). Another possibility to protect mRNAs from degradation is their decoration with ribosomes during translation which blocks access of RNases to cleavage sites within the RNA molecule (62,67). In this context, codon bias (i.e. the uneven use of synonymous codons in the genome) was shown to play a critical role for translation and mRNA turnover (68,69). Thus, rare codons are usually translated slower which causes pausing of the ribosomes, leading to stabilization of the mRNA by protecting the transcripts from RNases (68). Indeed, when performing a codon usage analysis (by employing the graphical codon usage analyzer 2.0 (70)) we identified a stretch of rare codons located within in the 3′ part of the *metF* gene (see Supplementary Figure S3 for details). 5′-RACE analysis showed that this region covers the majority of 5′-ends of the stable 3′-end transcript of the *metICFE-mdh* mRNA (Figure 7D). Thus, rare codon usage and protection by ribosomes might be involved in stabilization of the transcript towards the 3′-end. But, clearly more experimental work is needed to substantiate this hypothesis.

Met enzyme amounts are influenced by varying transcript and protein stabilities

Cellular protein levels are determined by a number of factors such as transcript availability and translation rate as well as by the stability of the synthesized protein. When quantifying intracellular levels of the single Met enzymes, we found considerable differences regarding relative protein amounts. Thus, enzymes engaged in the early steps of methionine biosynthesis such as transsulfuration (executed by MetI and MetC) are less abundant than MetE which performs the final and decisive methylation step to convert homocysteine into methionine, a reaction which is also involved in essential SAM recycling (Figure 10A). MetE is by far the most abundant protein encoded by the operon (i.e. 69 %). The enzyme represents a cobalamin-independent methionine synthase which, in *E. coli*, was described to be 100-fold less efficient than the cobalamin-dependent methionine synthase MetH (71). Under methionine-deprived conditions, MetE can account for up to 3% of total soluble protein in *E. coli* to compensate for the low efficiency of the enzyme (2,71,72). It is reasonable to suggest that staphylococci may accumulate high intracellular MetE levels for the same reason, for instance through stabilizing its mRNA. Indeed, when determining the protein synthesis rates after transcription arrest we found enzymes encoded towards the stable 3′-end of the *met* operon mRNA (i.e. MetE, Mdh) to have higher synthesis rates than those located at the instable 5′ end (i.e. MetI, MetC, MetF) (Figure 10D). However, transcript stability and protein synthesis rates are not the only factors influencing cellular protein amounts. In this respect, protein degradation is another important checkpoint and when determining the half-lives of the Met enzymes we found significant differences regarding individual Met enzyme stabilities (Figure 10C). Thus, for example, MetI has a long half-life (i.e. 7.2 h) and it is tempting to speculate that this might compensate for localization of the *metI* gene in the extremely short-lived 5′-portion of the transcript and the low protein synthesis rate (Figure 10D). Interestingly, not all of the enzymes encoded by the *met* operon seem to follow such a clear relationship between gene position, synthesis rate, protein stability and the detectable amount of protein. For example, Mdh (a protein of so far unknown function) which is encoded together with MetE in the stable 3′ transcript part, displays a similar protein synthesis rate as MetE. Despite of this and a very long Mdh half-life, the protein is by far less abundant than MetE (i.e. 11% versus 69%) (Figure 10A, C, D). The combined data suggest that transcript and protein stability are important, but certainly not the sole factors that adjust enzyme amounts to current metabolic requirements. Clearly, more future work is needed to fully understand staphylococcal methionine biosynthesis, for instance by addressing other regulatory levels such as translation initiation, enzyme activities and allosteric feedback control.

CONCLUSIONS

The strictly methionine-dependent and complex regulation of *de novo* methionine biosynthesis, involving a hierarchical string of regulatory cues, is probably due to the fact that staphylococci lack important methionine recycling pathways. Staphylococci therefore avoid overproduction of this metabolically costly amino acid. Coordinated mRNA decay seems to significantly contribute to the control of the pathway, thereby adding another layer of complexity to this sophisticated regulatory network. From an evolutionary point of view it is remarkable that staphylococci are the only genus among the Bacillales family to employ a T-box riboswitch to control the pathway. Even more astonishing, however, is the fact that this distinct MET-T-box riboswitch has unique structural features that distinguish it both from other methionyl-tRNA-specific systems as well as from T-box riboswitches in general. Notably, the unique terminator stem structure which renders this MET-T-box riboswitch an RNase III target, seems to be the key structural feature that sparks subsequent RNA decay events. Revealing the further details of this process, particularly regarding the mechanisms that stabilize the *met* operon mRNA towards the 3′-end, are interesting future experimental tasks.

DATA AVAILABILITY

Mass spectrometry data have been deposited to the ProteomeXchange Consortium via the PRIDE partner repository (73). Data received from protein quantification and half-life determination experiments can be obtained with the dataset identifier PXD020619. Data of the proteome

analysis for protein synthesis rate determination can be found with the dataset identifier PXD022677.

SUPPLEMENTARY DATA

Supplementary Data are available at NAR Online.

ACKNOWLEDGEMENTS

We are grateful to Peter Redder for providing the *rnj* mutants of *S. aureus* SA564RD, Christiane Wolz for providing the *rnc*, *rny* and *rnjB* mutants of *S. aureus* Newman and Isabelle Caldelari for providing the *rnc* mutant of *S. aureus* HG001. We also thank Tan Hock Siew for providing initial training with in-line probing. We thank Jürgen Bartel, Christine Wünsche and Thomas Sura for sample preparation prior to MS-analysis and MS-measurements.

FUNDING

German Research Council (DFG) through SPP1617 [ZI 665/2]; Transregional Collaborative Research Centre 34 [INST 292/67, B04]; ShARE [ZI665/3-1]; German Federal Ministry of Education and Research (BMBF) [01KI1727E, 16GW0297]. Funding for open access charge: German Research Council (DFG).
Conflict of interest statement. None declared.

REFERENCES

1. Wencker,F. and Ziebuhr,W. (2017) Chapter 13: methionine synthesis in microbes. In: *The Handbook of Microbial Metabolism of Amino Acids*. CABI, Oxfordshire, pp. 179–197.
2. Rodionov,D.A., Vitreschak,A.G., Mironov,A.A. and Gelfand,M.S. (2004) Comparative genomics of the methionine metabolism in Gram-positive bacteria: a variety of regulatory systems. *Nucl. Acids Res.*, **32**, 3340–3353.
3. Kaleta,C., Schäuble,S., Rinas,U. and Schuster,S. (2013) Metabolic costs of amino acid and protein production in *Escherichia coli*. *Biotechnol. J.*, **8**, 1105–1114.
4. Sekowska,A., Ashida,H. and Danchin,A. (2019) Revisiting the methionine salvage pathway and its paralogues. *Microb. Biotechnol.*, **12**, 77–97.
5. Joshi,G.S., Spontak,J.S., Klapper,D.G. and Richardson,A.R. (2011) Arginine catabolic mobile element encoded *speG* abrogates the unique hypersensitivity of *Staphylococcus aureus* to exogenous polyamines. *Mol. Microbiol.*, **82**, 9–20.
6. Schoenfelder,S.M.K., Marincola,G., Geiger,T., Goerke,C., Wolz,C. and Ziebuhr,W. (2013) Methionine biosynthesis in *Staphylococcus aureus* is tightly controlled by a hierarchical network involving an initiator tRNA-Specific T-box riboswitch. *PLoS Pathog.*, **9**, e1003606.
7. Geiger,T. and Wolz,C. (2014) Intersection of the stringent response and the CodY regulon in low GC Gram-positive bacteria. *Int. J. Med. Microbiol.*, **304**, 150–155.
8. Suddala,K.C. and Zhang,J. (2019) An evolving tale of two interacting RNAs—themes and variations of the T-box riboswitch mechanism. *IUBMB Life*, **71**, 1167–1180.
9. Kreuzer,K.D. and Henkin,T.M. (2018) The T-box riboswitch: tRNA as an effector to modulate gene regulation. *Microbiol. Spectrum*, **6**, RWR-0028-2018.
10. Zhang,J. and Ferré-D'Amaré,A.R. (2013) Co-crystal structure of a T-box riboswitch stem I domain in complex with its cognate tRNA. *Nature*, **500**, 363–366.
11. Zhang,J., Chetnani,B., Cormack,E.D., Alonso,D., Liu,W., Mondragón,A. and Fei,J. (2018) Specific structural elements of the T-box riboswitch drive the two-step binding of the tRNA ligand. *eLife*, **7**, e39518.
12. Vitreschak,A.G., Mironov,A.A., Lyubetsky,V.A. and Gelfand,M.S. (2008) Comparative genomic analysis of T-box regulatory systems in bacteria. *RNA*, **14**, 717–735.
13. Bae,T. and Schneewind,O. (2006) Allelic replacement in *Staphylococcus aureus* with inducible counter-selection. *Plasmid*, **55**, 58–63.
14. Geiger,T., Francois,P., Liebeke,M., Fraunholz,M., Goerke,C., Krismer,B., Schrenzel,J., Lalk,M. and Wolz,C. (2012) The stringent response of *Staphylococcus aureus* and its impact on survival after phagocytosis through the induction of intracellular PSMs expression. *PLoS Pathog.*, **8**, e1003016.
15. Lerch,M.F., Schoenfelder,S.M.K., Marincola,G., Wencker,F.D.R., Eckart,M., Förstner,K.U., Sharma,C.M., Thormann,K.M., Kucklick,M., Engelmann,S. *et al.* (2019) A non-coding RNA from the intercellular adhesion (*ica*) locus of *Staphylococcus epidermidis* controls polysaccharide intercellular adhesion (PIA)-mediated biofilm formation. *Mol. Microbiol.*, **111**, 1571–1591.
16. Schindelin,J., Arganda-Carreras,I., Frise,E., Kaynig,V., Longair,M., Pietzsch,T., Preibisch,S., Rueden,C., Saalfeld,S., Schmid,B. *et al.* (2012) Fiji: an open-source platform for biological-image analysis. *Nat. Methods*, **9**, 676–682.
17. Brenneis,M., Hering,O., Lange,C. and Soppa,J. (2007) Experimental characterization of cis-acting elements important for translation and transcription in halophilic archaea. *PLos Genet.*, **3**, e229.
18. Marincola,G., Schäfer,T., Behler,J., Bernhardt,J., Ohlsen,K., Goerke,C. and Wolz,C. (2012) RNase Y of *Staphylococcus aureus* and its role in the activation of virulence genes. *Mol. Microbiol.*, **85**, 817–832.
19. Monk,I.R., Shah,I.M., Xu,M., Tan,M.-W. and Foster,T.J. (2012) Transforming the untransformable: application of direct transformation to manipulate genetically *Staphylococcus aureus* and *Staphylococcus epidermidis*. *MBio*, **3**, e00277-11.
20. Nair,D., Memmi,G., Hernandez,D., Bard,J., Beaume,M., Gill,S., Francois,P. and Cheung,A.L. (2011) Whole-genome sequencing of *Staphylococcus aureus* strain RN4220, a key laboratory strain used in virulence research, identifies mutations that affect not only virulence factors but also the fitness of the strain. *J. Bacteriol.*, **193**, 2332–2335.
21. Baba,T., Bae,T., Schneewind,O., Takeuchi,F. and Hiramatsu,K. (2008) Genome sequence of *Staphylococcus aureus* strain Newman and comparative analysis of staphylococcal genomes: polymorphism and evolution of two major pathogenicity islands. *J. Bacteriol.*, **190**, 300–310.
22. Redder,P. and Linder,P. (2012) New range of vectors with a stringent 5-fluoroorotic acid-based counterselection system for generating mutants by allelic replacement in *Staphylococcus aureus*. *Appl. Environ. Microbiol.*, **78**, 3846–3854.
23. Herbert,S., Ziebandt,A.-K., Ohlsen,K., Schäfer,T., Hecker,M., Albrecht,D., Novick,R. and Götz,F. (2010) Repair of global regulators in *Staphylococcus aureus* 8325 and comparative analysis with other clinical isolates. *Infect. Immun.*, **78**, 2877–2889.
24. Caldelari,I., Chane-Woon-Ming,B., Noirot,C., Moreau,K., Romby,P., Gaspin,C. and Marzi,S. (2017) Complete genome sequence and annotation of the *Staphylococcus aureus* strain HG001. *Genome Announc.*, **5**, e00783-17.
25. Lalaouna,D., Baude,J., Wu,Z., Tomasini,A., Chicher,J., Marzi,S., Vandenesch,F., Romby,P., Caldelari,I. and Moreau,K. (2019) RsaC sRNA modulates the oxidative stress response of *Staphylococcus aureus* during manganese starvation. *Nucleic Acids Res.*, **47**, 9871–9887.
26. Oun,S., Redder,P., Didier,J.-P., François,P., Corvaglia,A.-R., Buttazzoni,E., Giraud,C., Girard,M., Schrenzel,J. and Linder,P. (2013) The CshA DEAD-box RNA helicase is important for quorum sensing control in *Staphylococcus aureus*. *RNA Biology*, **10**, 157–165.
27. Cox,J. and Mann,M. (2008) MaxQuant enables high peptide identification rates, individualized p.p.b.-range mass accuracies and proteome-wide protein quantification. *Nat. Biotechnol.*, **26**, 1367–1372.
28. Cox,J., Neuhauser,N., Michalski,A., Scheltema,R.A., Olsen,J.V. and Mann,M. (2011) Andromeda: a peptide search engine integrated into the MaxQuant environment. *J. Proteome Res.*, **10**, 1794–1805.
29. Saeed,A. i., Sharov,V., White,J., Li,J., Liang,W., Bhagabati,N., Braisted,J., Klapa,M., Currier,T., Thiagarajan,M. *et al.* (2003) TM4: a free, open-source system for microarray data management and analysis. *BioTechniques*, **34**, 374–378.

30. Silva,J.C., Gorenstein,M.V., Li,G.-Z., Vissers,J.P.C. and Geromanos,S.J. (2006) Absolute quantification of proteins by LCMSE : a virtue of parallel ms acquisition. *Mol. Cell. Proteomics*, **5**, 144–156.
31. Regulski,E.E. and Breaker,R.R. (2008) In-line probing analysis of riboswitches. *Methods Mol. Biol.*, **419**, 53–67.
32. Zuker,M. (2003) Mfold web server for nucleic acid folding and hybridization prediction. *Nucleic Acids Res.*, **31**, 3406–3415.
33. Winkler,W.C., Grundy,F.J., Murphy,B.A. and Henkin,T.M. (2001) The GA motif: an RNA element common to bacterial antitermination systems, rRNA, and eukaryotic RNAs. *RNA*, **7**, 1165–1172.
34. Grigg,J.C. and Ke,A. (2013) Sequence, structure, and stacking: specifics of tRNA anchoring to the T box riboswitch. *RNA Biol*, **10**, 1761–1764.
35. Durand,S. and Condon,C. (2018) RNases and helicases in gram-positive bacteria. *Microbiol. Spectrum*, **6(2)**, RWR-0003-2017.
36. Shahbabian,K., Jamalli,A., Zig,L. and Putzer,H. (2009) RNase Y, a novel endoribonuclease, initiates riboswitch turnover in *Bacillus subtilis*. *EMBO J.*, **28**, 3523–3533.
37. Khemici,V., Prados,J., Linder,P. and Redder,P. (2015) Decay-initiating endoribonucleolytic cleavage by RNase Y is kept under tight control via sequence preference and Sub-cellular localisation. *PLos Genet.*, **11**, e1005577.
38. Lioliou,E., Sharma,C.M., Caldelari,I., Helfer,A.-C., Fechter,P., Vandenesch,F., Vogel,J. and Romby,P. (2012) Global regulatory functions of the *Staphylococcus aureus* endoribonuclease III in gene expression. *PLos Genet.*, **8**, e1002782.
39. Romilly,C., Chevalier,C., Marzi,S., Masquida,B., Geissmann,T., Vandenesch,F., Westhof,E. and Romby,P. (2012) Loop-loop interactions involved in antisense regulation are processed by the endoribonuclease III in *Staphylococcus aureus*. *RNA Biology*, **9**, 1461–1472.
40. Gan,J., Tropea,J.E., Austin,B.P., Court,D.L., Waugh,D.S. and Ji,X. (2006) Structural insight into the mechanism of double-stranded RNA processing by Ribonuclease III. *Cell*, **124**, 355–366.
41. Michalik,S., Bernhardt,J., Otto,A., Moche,M., Becher,D., Meyer,H., Lalk,M., Schurmann,C., Schlüter,R., Kock,H. *et al.* (2012) Life and death of proteins: a case study of glucose-starved *Staphylococcus aureus*. *Mol. Cell. Proteomics*, **11**, 558–570.
42. Vitreschak,A.G., Rodionov,D.A., Mironov,A.A. and Gelfand,M.S. (2004) Riboswitches: the oldest mechanism for the regulation of gene expression? *Trends Genet.*, **20**, 44–50.
43. Grigg,J.C., Chen,Y., Grundy,F.J., Henkin,T.M., Pollack,L. and Ke,A. (2013) T box RNA decodes both the information content and geometry of tRNA to affect gene expression. *Proc. Natl Acad. Sci. U.S.A.*, **110**, 7240–7245.
44. Lehmann,J., Jossinet,F. and Gautheret,D. (2013) A universal RNA structural motif docking the elbow of tRNA in the ribosome, RNAse P and T-box leaders. *Nucleic Acids Res.*, **41**, 5494–5502.
45. Wang,J., Henkin,T.M. and Nikonowicz,E.P. (2010) NMR structure and dynamics of the specifier loop domain from *the Bacillus subtilis tyrS* T box leader RNA. *Nucleic Acids Res.*, **38**, 3388–3398.
46. Wang,J. and Nikonowicz,E.P. (2011) Solution structure of the K-turn and specifier loop domains from the *Bacillus subtilis tyrS* T-box leader RNA. *J. Mol. Biol.*, **408**, 99–117.
47. Grigg,J.C. and Ke,A. (2013) Structural determinants for geometry and information decoding of tRNA by T box leader RNA. *Structure*, **21**, 2025–2032.
48. Zhang,J. (2020) Unboxing the T-box riboswitches—a glimpse into multivalent and multimodal RNA–RNA interactions. *WIREs RNA*, **11**, e1600.
49. Sherwood,A.V., Frandsen,J.K., Grundy,F.J. and Henkin,T.M. (2018) New tRNA contacts facilitate ligand binding in a *Mycobacterium smegmatis* T box riboswitch. *Proc. Natl Acad. Sci. U.S.A.*, **115**, 3894–3899.
50. Battaglia,R.A., Grigg,J.C. and Ke,A. (2019) Structural basis for tRNA decoding and aminoacylation sensing by T-box riboregulators. *Nat. Struct. Mol. Biol.*, **26**, 1106–1113.
51. Suddala,K.C. and Zhang,J. (2019) High-affinity recognition of specific tRNAs by an mRNA anticodon-binding groove. *Nat. Struct. Mol. Biol.*, **26**, 1114–1122.
52. Yousef,M.R., Grundy,F.J. and Henkin,T.M. (2003) tRNA requirements for *glyQS* antitermination: a new twist on tRNA. *RNA*, **9**, 1148–1156.
53. Zhang,J. and Ferré-DAmaré,A.R. (2016) Trying on tRNA for size: RNase P and the T-box riboswitch as molecular rulers. *Biomolecules*, **6**, 18.
54. Apostolidi,M., Saad,N.Y., Drainas,D., Pournaras,S., Becker,H.D. and Stathopoulos,C. (2015) A *glyS* T-box riboswitch with species-specific structural features responding to both proteinogenic and nonproteinogenic tRNAGly isoacceptors. *RNA*, **21**, 1790–1806.
55. Zhang,J. and Ferré-D'Amaré,A.R. (2015) Structure and mechanism of the T-box riboswitches. *WIREs RNA*, **6**, 419–433.
56. Stamatopoulou,V., Apostolidi,M., Li,S., Lamprinou,K., Papakyriakou,A., Zhang,J. and Stathopoulos,C. (2017) Direct modulation of T-box riboswitch-controlled transcription by protein synthesis inhibitors. *Nucleic Acids Res.*, **45**, 10242–10258.
57. Frohlich,K.M., Weintraub,S.F., Bell,J.T., Todd,G.C., Väre,V.Y.P., Schneider,R., Kloos,Z.A., Tabe,E.S., Cantara,W.A., Stark,C.J. *et al.* (2019) Discovery of small-molecule antibiotics against a unique tRNA-Mediated regulation of transcription in gram-positive bacteria. *Chem. Med. Chem.*, **14**, 758–769.
58. Orac,C.M., Zhou,S., Means,J.A., Boehm,D., Bergmeier,S.C. and Hines,J.V. (2011) Synthesis and stereospecificity of 4,5-disubstituted oxazolidinone ligands binding to T-box riboswitch RNA. *J. Med. Chem.*, **54**, 6786–6795.
59. Deigan,K.E. and Ferré-D'Amaré,A.R. (2011) Riboswitches: discovery of drugs that target bacterial gene-regulatory RNAs. *Acc. Chem. Res.*, **44**, 1329–1338.
60. Seif,E. and Altman,S. (2008) RNase P cleaves the adenine riboswitch and stabilizes *pbuE* mRNA in *Bacillus subtilis*. *RNA*, **14**, 1237–1243.
61. Condon,C., Putzer,H. and Grunberg-Manago,M. (1996) Processing of the leader mRNA plays a major role in the induction of *thrS* expression following threonine starvation in *Bacillus subtilis*. *Proc. Natl Acad. Sci. U.S.A.*, **93**, 6992–6997.
62. Dar,D. and Sorek,R. (2018) Extensive reshaping of bacterial operons by programmed mRNA decay. *PLos Genet.*, **14**, e1007354.
63. Newbury,S.F., Smith,N.H. and Higgins,C.F. (1987) Differential mRNA stability controls relative gene expression within a polycistronic operon. *Cell*, **51**, 1131–1143.
64. Belasco,J.G., Beatty,J.T., Adams,C.W., Gabain,A. and Cohen,S.N. (1985) Differential expression of photosynthesis genes in *R. capsulata* results from segmental differences in stability within the polycistronic *rxcA* transcript. *Cell*, **40**, 171–181.
65. Båga,M., Göransson,M., Normark,S. and Uhlin,B.E. (1988) Processed mRNA with differential stability in the regulation of *E. coli* pilin gene expression. *Cell*, **52**, 197–206.
66. Marincola,G. and Wolz,C. (2017) Downstream element determines RNase Y cleavage of the *saePQRS* operon in *Staphylococcus aureus*. *Nucleic Acids Res.*, **45**, 5980–5994.
67. Deana,A. and Belasco,J.G. (2005) Lost in translation: the influence of ribosomes on bacterial mRNA decay. *Genes Dev.*, **19**, 2526–2533.
68. Boël,G., Letso,R., Neely,H., Price,W.N., Wong,K.-H., Su,M., Luff,J.D., Valecha,M., Everett,J.K., Acton,T.B. *et al.* (2016) Codon influence on protein expression in *E. coli* correlates with mRNA levels. *Nature*, **529**, 358–363.
69. Hanson,G. and Coller,J. (2018) Codon optimality, bias and usage in translation and mRNA decay. *Nat. Rev. Mol. Cell Biol.*, **19**, 20–30.
70. Fuhrmann,M., Hausherr,A., Ferbitz,L., Schödl,T., Heitzer,M. and Hegemann,P. (2004) Monitoring dynamic expression of nuclear genes in *Chlamydomonas reinhardtii* by using a synthetic luciferase reporter gene. *Plant Mol. Biol.*, **55**, 869–881.
71. Whitfield,C.D., Steers,E.J. and Weissbach,H. (1970) Purification and properties of 5-Methyltetrahydropteroyltriglutamate-homocysteine transmethylase. *J. Biol. Chem.*, **245**, 390–401.
72. Figge,R.M. (2007) Methionine biosynthesis in *Escherichia coli* and *Corynebacterium glutamicum*. In: Wendisch,V.F. (ed). *Amino Acid Biosynthesis Pathways, Regulation and Metabolic Engineering, Microbiology Monographs*. Springer Berlin Heidelberg, Berlin, Heidelberg, pp. 163–193.
73. Vizcaíno,J.A., Csordas,A., del-Toro,N., Dianes,J.A., Griss,J., Lavidas,I., Mayer,G., Perez-Riverol,Y., Reisinger,F., Ternent,T. *et al.* (2016) 2016 update of the PRIDE database and its related tools. *Nucleic Acids Res.*, **44**, D447–D456.